PERFORMANCE LIMITS OF SINGLE MOLECULE FLUORESCENCE MICROSCOPY IN TWO AND THREE DIMENSIONS

A Dissertation

by

AMIR TAHMASBI

Submitted to the Office of Graduate and Professional Studies of
Texas A&M University
in partial fulfillment of the requirements for the degree of

DOCTOR OF PHILOSOPHY

Chair of Committee,	Raimund J. Ober
Committee Members,	Brian E. Applegate
	Javier A. Jo
	E. Sally Ward
Head of Department,	Anthony Guiseppi-Elie

May 2017

Major Subject: Biomedical Engineering

Copyright 2017 Amir Tahmasbi

ABSTRACT

Photon-limited imaging is a core tool for the acquisition of precise quantitative data in a wide range of scientific endeavors, where parameters of an experiment are estimated. An important example is single molecule fluorescence microscopy, a relatively new optical microscopy technique that allows the detection of individual molecules such as proteins in a cellular context. One of the central aspects of such photon-limited imaging systems concerns the lowest possible variance with which an unknown parameter, e.g. the location of an object, can be estimated. The Cramér–Rao Lower Bound (CRLB) on the variance of unbiased estimators is widely used to assess the performance limits of imaging systems. However, the current approach for the calculation of the CRLB relies on an analytical expression for the image of the object. This can pose practical challenges since it is typically difficult to find appropriate analytical models for the images of general objects. Here, we instead develop an approach that directly uses an experimentally collected image set to calculate the CRLB for the location of a general object. In this approach, we fit splines, i.e. smoothly connected piecewise polynomials, to the experimentally acquired image set to provide a continuous model of the object, which can then be used for the calculation of the CRLB. Due to its practical importance, we investigated in detail the application of the proposed approach in single molecule microscopy.

Another contribution of this dissertation is the development of techniques based on the CRLB for the design of plane spacing for Multifocal Plane Microscopy (MUM). MUM is a 3D imaging modality that allows the study of subcellular dynamics in 3D at high temporal and spatial resolution by simultaneously imaging distinct planes within the specimen. An important question in MUM experiments is how the number of focal planes and their spacings should be chosen to achieve the best possible localization accuracy. Here, we report spacing scenarios that yield an appropriate 3D localization accuracy. We investigated the effect of the number of focal planes on the 3D localization accuracy. Additionally, we introduced a software package for designing the plane spacings for a MUM setup.

To my family

ACKNOWLEDGEMENTS

I would like to express my gratitude to my supervising professors, Drs. Raimund J. Ober and E. Sally Ward, for their advice and support during my doctoral studies. I have learned a lot in the last five years and I thank them for giving me the opportunity to work in their lab. I would like to thank my committee members, Drs. Brian E. Applegate and Javier A. Jo, for taking the time to serve on my committee.

Additionally, I would like to extend my appreciation to all current and former members of the Ward Ober Lab who have created a productive work environment. In particular, I would like to thank our lab manager, Dr. Rafal Swiercz, for excellent logistical support, as well as Drs. Ed Cohen, Sripad Ram and Jerry Chao for reviewing my manuscripts. Special thanks are due to my colleagues Zita and Siva, among others who have been a great support during my PhD.

I would like to thank my department head, Dr. Guiseppi-Elie, for his invaluable help and support in difficult times, and for teaching me to take action towards my dreams. Finally, I would like to express my deep gratitude to my girlfriend Kimia and my family, for all their support. In particular, this PhD would have been impossible without Kimia's love and constant support.

I want to close with my favorite quote from Mahatma Gandhi: "*It's the action, not the fruit of the action, that's important. You have to do the right thing. It may not be in your power, may not be in your time, that there'll be any fruit. But that doesn't mean you stop doing the right thing. You may never know what results come from your action. But if you do nothing, there will be no result.*" I hope readers of this dissertation will be moved to action of some sort.

October 15, 2016

CONTRIBUTORS AND FUNDING SOURCES

Contributors

This work was supported by a dissertation committee consisting of Professors Raimund Ober, Javier Jo and Brian Applegate of the Department of Biomedical Engineering and Professor Sally Ward of the Department of Cellular and Molecular Medicine.

Professor Ober helped significantly with the research, preparation, writing, and reviewing the manuscripts which led to the contents of this dissertation. Professor Ward, Drs. Jerry Chao and Sripad Ram reviewed the manuscripts which led to the contents of this dissertation. In particular, I would like to acknowledge the following individuals for their assistance with the manuscript that forms Chapter 2 of this dissertation. The experimental data sets were acquired by Dongyoung Kim. The software for the simulation of the spherical shell was provided by Dr. Chao. Related to the work presented in Chapter 3, I would like to thank Dr. Chao for letting me take over the project after his initial work on it and for feedback and help in the remaining stages of the research. I would like to acknowledge the significant contribution towards the software by Felix Tang and Anish Abraham. I am grateful to Dr. Ram for writing part of the manuscript and his invaluable help with the project.

All other work conducted for the dissertation was completed by the student independently in the joint laboratory of Professors Ober and Ward.

Funding Sources

This work was made possible in part by National Institutes of Health under Grant Number R01 GM085575.

Its contents are solely the responsibility of the authors and do not necessarily represent the official views of the National Institutes of Health.

NOMENCLATURE

2D	Two-Dimensional
3D	Three-Dimensional
CCD	Charge Coupled Device
CMOS	Complementary Metal Oxide Semiconductor
CRLB	Cramér-Rao Lower Bound
EMCCD	Electron Multiplying Charge Coupled Device
FIM	Fisher Information Matrix
GFP	Green Fluorescent Protein
MUM	Multifocal Plane Microscopy
PALM	Photo-Activated Localization Microscopy
pdf	probability density function
PLAM	Practical Localization Accuracy Measure
PSF	Point Spread Function
RFP	Red Fluorescent Protein
RMSPE	Root Mean Square Percentage Error
ROI	Region Of Interest
STORM	Stochastic Optical Reconstruction Microscopy
uFIM	unit photon count Fisher Information Matrix
w.r.t.	with respect to

TABLE OF CONTENTS

LIST OF FIGURES

1. INTRODUCTION*

1.1 The importance of fluorescence microscopy

Optical microscopy has a long history going back several centuries during which it was a key technique for the discovery of biological processes [1]. The basic optical principles have not changed, but what has changed in the instrumentation in recent decades is the availability of highly sensitive detectors, computer control and powerful laser-based light sources [2,3]. With these improvements in instrumentation came the possibility to analyze the acquired microscopy data using advanced signal and image processing techniques (see e.g. [4,5]). Equally important, however, are the major advances in molecular biology and physical chemistry that have drastically improved the available technology for the labeling of cellular specimens [6–8].

These technological developments coincided with a time when the revolution in molecular biology has demanded powerful exploratory tools for the investigation of molecular processes in cells [2,8]. For example, through genomic analyses, biologists have identified a large array of proteins, such as growth factor receptors, that are known to play a role in cancer. Standard techniques in molecular biology and biophysics, e.g. X-ray crystallography, allow the study of these proteins to a very high level of detail. However, to investigate their biological functions, it is important that these proteins are studied in their cellular context.

Fluorescence microscopy is the imaging technique of choice for the study of molecular processes within cells due to its ability to detect specifically labeled proteins, receptors, molecules or structures [3,8,9]. There are, however, two aspects of fluorescence microscopy that limit its power. The first aspect is the spatial resolution of optical microscopy, which is a measure of the ability to distinguish two closely spaced point-like objects [10]. While

---

[*] Part of this chapter is reprinted with minor modifications, with permission from "Quantitative aspects of single molecule microscopy: information-theoretic analysis of single-molecule data" by R. J. Ober, A. Tahmasbi, S. Ram, Z. Lin, and E. S. Ward, 2015. IEEE Signal Process. Mag., vol. 32, no. 1, pp. 58-69, Copyright 2015 by IEEE.

molecular interactions occur on the low nanometer scale, classical resolution criteria predict a resolution limit in the range of several hundred nanometers [10–12]. The second aspect is the sensitivity of the technique. A fluorescent molecule emits only a limited number of photons [2,13]. This fact, together with the limited resolution of an optical microscope, implies that in classical fluorescence microscopy only relatively large accumulations of fluorescent molecules are detected. These detection limitations of classical fluorescence microscopy and in particular their associated averaging effects stand in the way of examining the molecular processes and structures at the level of individual molecules, i.e. precisely at the level that is required to study these phenomena in their full detail.

1.2 Single molecule fluorescence microscopy

Single molecule (fluorescence) microscopy is a technique that promises to overcome the deficiencies of classical fluorescence microscopy by allowing the detection of individual molecules rather than larger accumulations of molecules [2,13]. Single molecule microscopy goes back to the work by W. E. Moerner and L. Kador published in 1989 [14], followed by that of M. Orrit and J. Bernard published in 1990 [15]. Amongst the many stages of development, we mention a few. In 1991, the image of a single molecule was recorded for the first time [16]. In 2003, single molecule microscopy played a crucial role in the measurement of the step size that the molecular motor myosin V takes in moving along an actin in an in vitro model [17]. This was based on being able to estimate the location of the myosin V molecule within 1.5 nm [17]. The Green Fluorescent Protein (GFP) brought about a major breakthrough in fluorescent microscopy of proteins in living cells as the protein of interest can be genetically tagged by the GFP gene [6, 7]. The first single molecule experiments in live cells using a GFP tag were reported in [18,19]. In a series of papers, it was recognized that the classical resolution criteria do not apply and distances well below those criteria can be measured using single molecule microscopy [11, 20, 21]. One of the key observations was that resolution is significantly improved if the molecules to be imaged are not excited at the same time [22]. Various photophysical processes were investigated such as blinking [21], photobleaching [20], and photoswitching [23]. This knowledge was exploited in [23–25] when it was recognized that various fluorophores can be stochastically excited which allows only a small number of the total fluorophores present in a sample to be imaged at any time point. This led to the development of localization based super-resolution microscopy techniques [23–25]. The development of techniques continues at a significant rate with the introduction of new approaches and refinements of existing ones.

To put the significance of single molecule microscopy in context, we next discuss the principles behind two of the most important single molecule experiments. The first one, a single molecule tracking experiment, aims at obtaining the trajectories of individual molecules as they move in a cell [4, 5, 26–28]. The second one, a localization based super-resolution experiment aims to provide an image with a resolution well beyond what is achievable by classical methods [21, 23–25].

1.2.1 Tracking single molecules

The movement of molecules such as receptors and proteins in cells is crucial for the functioning of the cells [17, 26]. Despite the importance of these processes much remains unknown. Therefore, tracking experiments, i.e. experiments that record such dynamic behavior over time, are of particular importance [4]. In order to obtain the most detailed analysis, it is essential to carry out these experiments in live cells at the single molecule level (see Fig. 1.1).

Such single molecule tracking experiments, however, are not without significant challenges. Foremost amongst them is the need to be able to image isolated single molecules [4, 26] (see Fig. 1.1(a)). This can often be achieved with sparse labeling. Another significant problem is the photobleaching of many of the conventional fluorescent labels, which means that a fluorophore will only emit a certain, typically randomly distributed, number of photons before it ceases to emit photons [6, 7]. The phenomenon in effect limits the length of time for which the track of a single molecule can be followed.

In designing a single molecule tracking experiment a number of important trade-offs need to be made, in particular, regarding the frame rate of the acquisition and the associated exposure time for each of the images. High frame rates and corresponding short

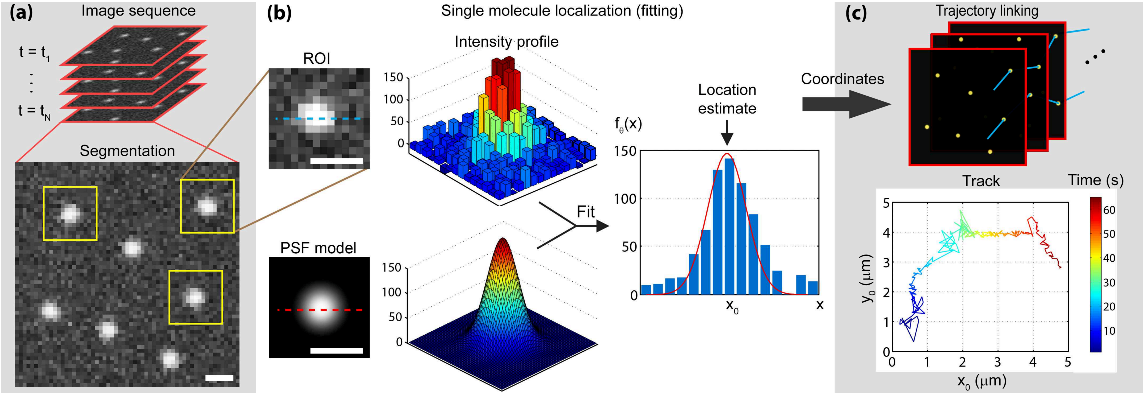

Figure 1.1: Single molecule tracking. (a) A sequence of images acquired at different time points are first segmented into multiple Regions of Interest (ROIs) each containing an isolated single molecule. (b) In the single molecule localization step, a Point Spread Function (PSF) model such as the Airy profile or a bivariate Gaussian distribution is fitted to each ROI to estimate the location of the single molecule with sub-pixel precision. This provides a set of coordinates of single molecules. (c) The set of coordinates together with their corresponding time points are then analyzed by a trajectory linking algorithm. In this way, the trajectory of each single molecule can be determined (a sample trajectory is shown). Size bars are 1 μm. Reprinted with permission from [1].

exposure times allow for better sampling of the dynamics of the single molecule. Reducing the exposure time, however, decreases the number of photons that are detected during the exposure interval and thereby, as will be shown later, will reduce the accuracy with which the parameters can be estimated that are associated with the trajectory [13, 26, 28]. Increasing the excitation light power could be used to increase the number of emitted photons per exposure. However, this will reduce the lengths of trajectories that can be imaged due to photobleaching. In addition, subjecting a cellular sample to excitation light that is too powerful might damage the living cell that is being imaged.

1.2.2 Localization-based superresolution microscopy

The second prototype experiment involves the imaging of fixed, i.e. dead, cells to obtain very high resolution information concerning subcellular structures. In a classical fluorescence microscopy experiment, all fluorophores are simultaneously excited and imaged with one single exposure. As explained earlier, with densely spaced fluorophores, the result

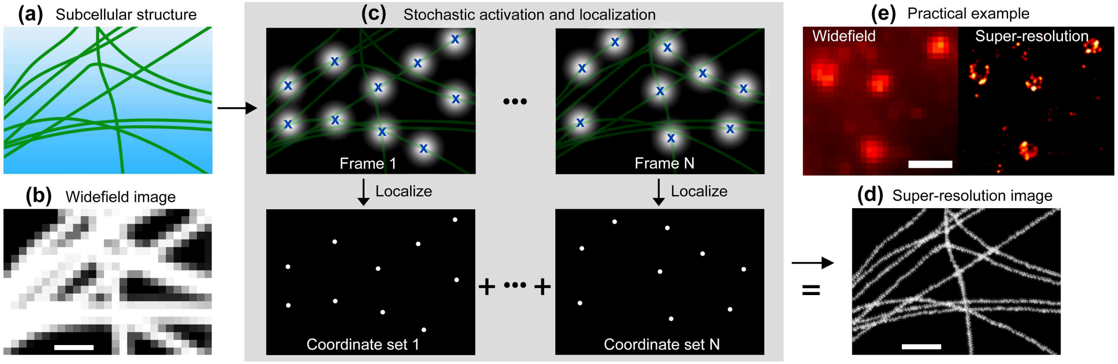

Figure 1.2: Localization based super-resolution microscopy. (a) The schematic shows a subcellular structure (a microtubule network) that is uniformly labeled with specific fluorophores. (b) In conventional imaging, all of the fluorophores in the sample are simultaneously excited. Due to the resolution limit of fluorescence microscope, the resulting widefield image is poorly resolved and fails to reveal the underlying structure in the sample. (c) In localization based super-resolution microscopy, the imaging conditions facilitate activation of random subsets of fluorophores that are typically spatially well separated. These fluorophores are then localized with sub-pixel precision and their coordinates are then used to create a super-resolution image of the sample. (d) The resulting super-resolution image provides fine structural information of the sample that is not accessible through a widefield image. (e) Comparison of a practical widefield image and a super-resolution image. In panel (e), the size bar is 2 μm. In all other panels, size bars are 300 nm. Reprinted with permission from [1].

is that the individual fluorophores cannot be distinguished in the acquired image (see e.g. Fig. 1.2(a) and (b)). The idea that underlies localization based super-resolution microscopy is to image the sample a large number of times, but in each of the images that make up the full acquisition set, only a small and sparse subset of the fluorophores is imaged (see Fig. 1.2(c)) [23, 24]. Through a particular choice of fluorescent labels, appropriate sample preparation and laser excitation, such sparse, random activation can in fact be achieved. The resulting images each are designed such that the positions of the sparsely located single molecules can be accurately determined. For each of the typically thousands of images, the locations of the single molecules are estimated [24, 25]. The final image is then assembled from the location estimates of the single molecules in each of the images (see Fig. 1.2(d)).

Different techniques are available to produce these sparse subsets of fluorophores. These are primarily based on the exploitation of new insights into the photophysics of fluorophores [20–22], whereby powerful excitation light sources can be used to stochastically excite subsets of fluorophores, put them in non-emitting states, or photobleach them. Depending on the specific mechanisms and fluorophores, these techniques are known as Photo-Activated Localization Microscopy (PALM), Stochastic Optical Reconstruction Microscopy (STORM), direct STORM, etc. [23–25].

1.3 Challenges in single molecule microscopy

Photon-limited imaging techniques, such as single molecule microscopy, place stringent demands on experimental and algorithmic tools due to the low signal levels and the presence of significant extraneous noise sources. Consequently, this has necessitated the use of advanced statistical signal and image processing techniques for the design and analysis of photon-limited imaging experiments. In this section, we provide an overview of a number of challenges in photon-limited imaging. While we mainly focus on the single molecule microscopy application, a number of these challenges are generally encountered in photon-limited imaging.

As we showed earlier, both the single molecule tracking and the localization based super-resolution experiments depend on the accurate determination of the locations of the imaged single molecules [4, 28, 29]. As such, a central question in single molecule microscopy concerns the best possible accuracy, in terms of standard deviation, with which the location of an object can be estimated [13]. The best possible localization accuracy is typically obtained using the Cramér–Rao Lower Bound (CRLB) [1, 30]. Theoretical lower bounds on the accuracy of estimates, such as the CRLB, are very useful in assessing the quantitative performance of systems as they can predict how well a system performs an estimation task without specifying a particular estimator [1, 30]. This feature has rendered the CRLB a reliable measure of accuracy that helps to optimize the design of single molecule microscopy experiments [1, 2, 30, 31].

The use of the CRLB in designing microscopy experiments, however, poses technical challenges in practice which have yet to be addressed. Importantly, the calculation of the

CRLB to date relied on an analytical expression for the image of the object, which we refer to as the image function [26,30,32]. In practice, this can be problematic owing to the fact that often no accurate analytical image function is available [33,34]. Even if an appropriate analytical model is available for the image function, the lack of knowledge about the precise values of imaging parameters might also impose difficulties in the calculation of the CRLB, as analytical image functions are typically functions of the imaging parameters [35]. This problem will be addressed by developing a new methodology for determining the CRLB directly from experimentally acquired image sets [34].

As mentioned earlier, high accuracy 3D tracking of single molecules, e.g. proteins, in live cells holds the promise to provide novel insights into subcellular processes, which otherwise cannot be gained through traditional experimental approaches [5,26]. For instance, in [32], 3D single molecule tracking of transferrin molecules over a 10-micrometer depth revealed rapid intercellular transferrin transport at live epithelial cell barriers. The study of such intracellular transport pathways is not only fundamental to understanding tissue homeostasis but is also of importance for targeted drug delivery across cellular barriers at specific body sites, such as the brain that is impermeable to blood-borne substances. To capture the full 3D dynamics of single molecules, it is necessary to accurately estimate their 3D locations over a large depth at high temporal resolution. This can typically be achieved through a 3D single molecule imaging modality, such as Multifocal Plane Microscopy (MUM). MUM allows the 3D tracking of single molecules at high spatial and temporal resolution by simultaneously imaging different focal planes within the sample (see Fig. 1.3) [31,36].

Designing MUM experiments, however, also poses technical challenges in practice which have yet to be addressed. The accuracy with which the 3D locations of the single molecules imaged using MUM can be estimated depends on the number of focal planes and their spacings [31, 37]. Therefore, it is of importance to determine the appropriate number of focal planes and their spacing to achieve the best possible 3D localization accuracy. To address this problem, by making use of the CRLB, we analyze the best theoretically

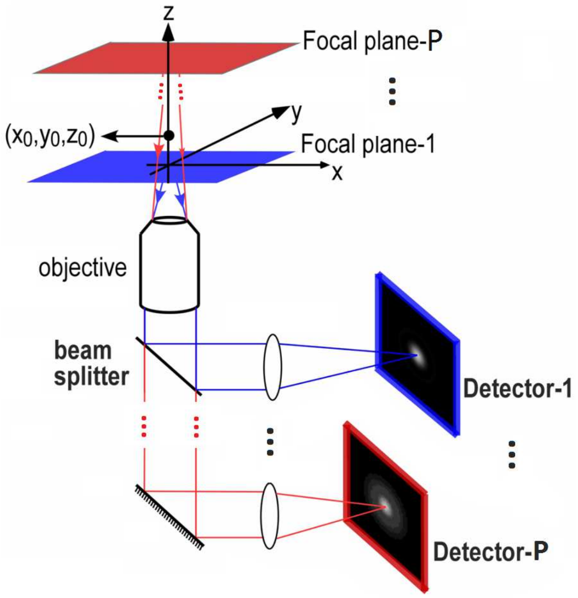

Figure 1.3: The schematic diagram of a P-plane MUM setup. The emitted photons form the sample are collected by the objective lens and are then split among different paths. The light in each path is focused onto a detector which is slightly shifted with respect to the detector associated with the standard infinity-corrected (i.e. design) focal plane.

possible 3D localization accuracy for a MUM setup along the z-axis and develop analytical and software tools to facilitate the plane spacing design process [31, 37].

1.4 Overview of the dissertation

This dissertation is organized as follows. In the next chapter, we develop a new methodology for determining the CRLB directly from experimentally acquired image sets, as opposed to analytical image functions. As will be shown later, a continuously differentiable representation of the experimental image set is necessary to obtain the derivatives which are required for the calculation of the CRLB. To achieve such a continuously differentiable model, we will fit splines, i.e. smoothly connected piecewise polynomials, to the experimentally acquired image set [38]. As such, the next chapter also explores splines and their properties, and describes how splines can help in finding the best possible localization accuracy given a practical imaging setup.

In Chapter 3, we direct our attention to the design of MUM experiments. We propose approaches based on the CRLB to investigate the number of focal planes and their spacings which provide the best possible localization accuracy along the z-axis. We report spacing scenarios called strong coupling and weak coupling which yield an appropriate 3D localization accuracy. We further examine the effect of imaging parameters, such as the numerical aperture of the objective lens, magnification, photon count, emission wavelength and extraneous noise on the spacing scenarios. In addition, we introduce a new software package that provides a user-friendly framework to find appropriate plane spacings for a MUM setup. These developments should assist in optimizing MUM experiments.

Chapter 4 presents the concluding remarks.

1.5 List of published papers

The following is a list of published journal articles during the course of the PhD studies. In addition to the papers listed below, I was involved in other projects that are not reported in this dissertation. Those projects will lead to additional publications in due course.

(J1) A. Tahmasbi, E. S. Ward, and R. J. Ober, "Determination of localization accuracy based on experimentally acquired image sets: applications to single molecule microscopy," *Opt. Express*, vol. 23, no. 6, pp. 7630-7652, 2015.

(J2) R. J. Ober, A. Tahmasbi, S. Ram, Z. Lin, and E. S. Ward, "Quantitative aspects of single molecule microscopy: information-theoretic analysis of single-molecule data," *IEEE Signal Process. Mag.*, vol. 32, no. 1, pp. 58-69, 2015.

(J3) A. Tahmasbi, S. Ram, J. Chao, A. V. Abraham, F. W. Tang, E. S. Ward, and R. J. Ober, "Designing the focal plane spacing for multifocal plane microscopy," *Opt. Express*, vol. 22, no. 14, pp. 16706-16721, 2014.

(J4) R. Swiercz, S. Chiguru, A. Tahmasbi, S. M. Ramezani, G. Hao, D. K. Challa, M. A. Lewis, P. V. Kulkarni, X. Sun, R. J. Ober, R. P. Mason, and E. S. Ward, "Use of Fc-engineered antibodies as clearing agents to increase contrast during PET," *J.*

Nucl. Med., vol. 55, no. 7, pp. 1204-1207, 2014.

The following is a list of published conference papers during the course of the PhD studies.

(C1) A. Tahmasbi, E. S. Ward, and R. J. Ober, "New results on the single molecule localization problem in two and three dimensions," in Proc. *SPIE, Nanoimaging and Nanospectroscopy III*, 9554: 955402, San Diego, CA, August 9, 2015.

(C2) A. Tahmasbi, S. Ram, J. Chao, A. V. Abraham, E. S. Ward, and R. J. Ober, "An information-theoretic approach to designing the focal plane spacing for multifocal plane microscopy," in Proc. *SPIE International Symposium on Biomedical and Optics*, 9330: 933011, San Francisco, CA, February 11, 2015.

2. DETERMINATION OF LOCALIZATION ACCURACY BASED ON EXPERIMENTALLY ACQUIRED IMAGE SETS*

2.1 Introduction

Fluorescence microscopy, a light microscopy technique that enables the detection of specifically-labeled objects, is extensively used to study subcellular structures, proteins and dynamics [1, 26, 39, 40]. An important question in fluorescence microscopy concerns the best possible accuracy, in terms of standard deviation, with which an object of interest can be localized. This is particularly important for applications such as localization-based superresolution microscopy in which the spatial resolution is closely related to the localization accuracy [1, 40]. This problem has been addressed by introducing the Practical Localization Accuracy Measure (PLAM) [13, 31, 41]. The PLAM provides a lower bound on the accuracy with which an unknown parameter, e.g. the location of a subcellular object or a single molecule, can be estimated when imaged using a pixelated detector [13,41]. The PLAM is calculated using a well-established statistical tool, the Cramér-Rao lower bound, that is, the inverse of the Fisher information [42, 43]. The latter represents the amount of information the data provides about an unknown parameter [42]. Lower bounds on the accuracy of estimates are useful in assessing the quantitative performance of systems as they can predict how well a system can perform an estimation task without specifying a particular estimator [12, 13, 42]. This feature has turned the PLAM into a reliable measure of accuracy that helps to optimize the design of fluorescence microscopy experiments [1, 12, 29, 44–47].

However, the calculation of the PLAM to date relied on an analytical expression for the image of the object, which we refer to as the image function [10, 12, 13]. In practice, this can be problematic owing to the fact that often no accurate analytical image function

---

*Reprinted with minor modifications, with permission from "Determination of localization accuracy based on experimentally acquired image sets: applications to single molecule microscopy" by A. Tahmasbi, E. S. Ward, and R. J. Ober, 2015. Opt. Express, vol. 23, no. 6, pp. 7630-7652, Copyright 2015 by Optical Society of America.

is available [10,33,48]. Even if an appropriate analytical model is available for the image function, the lack of knowledge about the precise values of imaging parameters might also impose difficulties in the calculation of the PLAM, as analytical image functions are typically strongly tied to the parameters of the imaging setup [12,26]. For instance, as shown in [35], the experimentally achievable value for the numerical aperture of an objective lens might considerably differ from its nominal value, especially for a high numerical aperture objective lens.

Here, we address the above concerns by developing a new approach that directly makes use of an experimental image set to calculate the PLAM for a general object. A continuously differentiable representation of the experimental image set is necessary to obtain certain derivatives that are required for the calculation of the PLAM. To achieve such a continuously differentiable model we fit splines, i.e. smoothly connected piecewise polynomials, to the experimentally collected image set [38,49–51]. We use splines since they are well-established in image processing [38,49,52] and have a number of useful properties. Importantly, their derivatives can be obtained analytically [49]. Our proposed method only requires the experimental image set and provides the best possible accuracy with which a general subcellular object can be localized [53]. Knowledge of imaging parameters such as the numerical aperture of the objective lens and the refractive index of the immersion oil is not required as these parameters are already encoded in the experimental image set.

Single molecule microscopy is a well-known application of fluorescence microscopy which allows the detection of individual molecules [13,39,40]. Due to its practical importance, we study the application of our approach to single molecule microscopy in more detail. In this case, the object of interest is a single molecule which is typically modeled as a point source [13,40] and, as such, the acquired image set pertains to an experimental PSF. An experimental PSF is a (3D) PSF obtained by (z-stack) imaging a point source, e.g. a bead [54–57]. We verify our approach using simulations in the presence of extraneous noise sources and give practical examples. We also give non-point source examples.

Although in this study we focus on fluorescence microscopy applications, our proposed approach is generally applicable to imaging problems, and can therefore also be utilized in other applications, e.g. astronomy.

2.2 Materials and methods

2.2.1 Acquisition of the experimental PSF

A bead sample was prepared using 0.1 μm Tetraspeck$^{\text{TM}}$ beads (Life Technologies Corporation, Grand Island, NY) as described in [58]. The imaging of the beads was carried out using a Zeiss Axiovert 200 inverted microscope with a Zeiss Plan-apochromat 63x, NA 1.45 oil immersion objective lens (Carl Zeiss, Oberkochen, Germany) at a refractive index of 1.515. The measurement of the 3D PSF was performed by z-stack imaging with a Piezo Flexure Objective Scanner (Physik Instrumente, Karlsruhe, Germany) with a step size of 25 nm. The sample was illuminated by a laser with a wavelength of 488 nm (Toptica Photonics, Munich, Germany) and the emission light (at a wavelength of 650 nm) was passed through a quad-band filter set (Semrock, Inc., Rochester, NY). An Electron Multiplying Charge Coupled Device (EMCCD) camera iXon DU897-BV (Andor Technologies, South Windsor, CT) with conventional readout and a pixel size of 16 μm × 16 μm was used to acquire the data.

2.2.2 Acquisition of the lysosome images

A human prostate carcinoma epithelial cell line, 22Rv1, was obtained from the ATCC (Manassas, VA) and was maintained in RPMI-1640 (Lonza, Basel, Switzerland) supplemented with 10 % FCS (HyClone Laboratories, Inc., Logan, UT). For imaging studies, the culture medium was replaced with phenol-red free RPMI-1640 (Invitrogen, Carlsbad, CA) supplemented with 10 % FCS (HyClone Laboratories, Inc.). The 22Rv1 cells were transfected with expression plasmids encoding LAMP-1 with C-terminally linked Red Fluorescent Protein (mRFP; [59]) using an Amaxa Nucleofector$^{\text{TM}}$ (Lonza) instrument and program X-001. 36 hours following transfection, the cells were imaged as live cells using a Zeiss Axio Observer A1 inverted microscope with a Zeiss Plan-apochromat 100x, NA 1.4 oil immersion objective lens (Carl Zeiss) at a refractive index of 1.515. The sample was illuminated by a 543 nm laser (Opto Engine LLC, Midvale, UT). A Charge Coupled Device (CCD) camera Orca ER (Hamamatsu, Bridgewater, NJ) with a pixel size of 6.45 μm × 6.45 μm was used to acquire the data.

2.2.3 Computations and software

All of the computations were carried out in a custom-written software package developed in the MATLAB environment (The MathWorks Inc., Natick, MA). This tool is capable of calculating the Fisher information matrix and the PLAM for both 2D and 3D experimental image sets.

2.3 Theory

2.3.1 Fisher information matrix and problem formulation

In this section, we briefly explain the theory for determining the best possible localization accuracy in single molecule microscopy. For a 3D localization problem, we denote the location of the object of interest in the object space by the parameter vector $\boldsymbol{\theta} := (x_0, y_0, z_0) \in \Theta$, where $\Theta \subseteq \mathbb{R}^3$, is an open parameter space. For a 2D localization problem, the location parameter vector is obviously reduced to $\boldsymbol{\theta} := (x_0, y_0) \in \Theta \subseteq \mathbb{R}^2$. The best possible accuracy with which the location of the object can be estimated, observing its pixelated image, is given by the PLAM [13,31,41]. The PLAM is determined using the CRLB [12,13]. According to the Cramér-Rao inequality [42,43], the covariance matrix of any unbiased estimator $\hat{\boldsymbol{\theta}}$ of a parameter vector $\boldsymbol{\theta} \in \Theta$ is always greater than or equal to the inverse Fisher Information Matrix (FIM), i.e.

$$\mathrm{cov}(\hat{\boldsymbol{\theta}}) \geq \boldsymbol{I}^{-1}(\boldsymbol{\theta}).$$

The main diagonal elements of the inverse FIM provide lower bounds on the variance of the estimates of the unknown parameters, whereas we are interested in the estimation accuracy in terms of the standard deviation. Hence, the PLAM vector is defined as the element-wise square root of the main diagonal entries of the inverse FIM [31,41].

We next express the FIM for the single molecule microscopy problem. Let $\{C_1, \ldots, C_{K_{\text{pix}}}\}$ be a pixelated detector, where $C_k \subseteq \mathbb{R}^2$ denotes the area occupied by the k^{th} pixel and K_{pix} is the total number of pixels. The pixels are assumed to be disjoint. It has been shown that the photon counts detected by the pixels of the detector due to the object of interest are the realizations of independent Poisson random variables with expected values [13, 43]

$$\mu_\theta(k) = \frac{N}{M^2} \int_{C_k} q_{z_0}\left(\frac{x}{M} - x_0, \frac{y}{M} - y_0\right) d\boldsymbol{r}, \qquad k = 1, \ldots, K_{\text{pix}}, \tag{2.1}$$

where $\boldsymbol{r} := (x, y) \in \mathbb{R}^2$, N is the expected number of photons that impact the infinite detector plane (i.e. $\mathbb{R}^2$) due to the object, M is the lateral magnification of the objective lens and q_{z_0} is the image function [12, 13]. The image function is a bivariate probability density function (pdf) that describes the image of a stationary object on the detector plane at unit lateral magnification when it is located on the optical axis at position $z_0 \in \mathbb{R}$ [1,12]. The image function for a 2D localization problem is simply given by setting $z_0 = 0$. In case that the object of interest is a point source, the image function is identical to the PSF of the optical system. For example, considering the standard Born and Wolf 3D PSF model [10], the image function is given by [26]

$$q_{z_0}(x, y) = A \left| \int_0^1 J_0\left(\frac{2\pi n_a}{\lambda} \rho \sqrt{x^2 + y^2}\right) e^{j \frac{\pi n_a^2 z_0}{\lambda n_{\text{oil}}} \rho^2} \rho d\rho \right|^2, \qquad (x, y) \in \mathbb{R}^2, \tag{2.2}$$

where A is a normalization constant, n_{oil} denotes the refractive index of the immersion medium, e.g. oil, and J_0 is the zeroth order Bessel function of the first kind [10].

It has been shown that in the presence of extraneous noise, the expression of the FIM is given by [12, 13]

$$\boldsymbol{I}(\boldsymbol{\theta}) = \sum_{k=1}^{K_{\text{pix}}} \frac{\alpha(k)}{v_\theta(k)} \left(\frac{\partial v_\theta(k)}{\partial \boldsymbol{\theta}}\right)^T \frac{\partial v_\theta(k)}{\partial \boldsymbol{\theta}}, \qquad \boldsymbol{\theta} \in \Theta, \tag{2.3}$$

where $v_\theta(k) := \mu_\theta(k) + b_k$ with $b_k,\ k = 1, \ldots, K_{\text{pix}}$, denoting the photon count due to the background signal at pixel C_k. If the parameter vector is independent of the background level b_k, we have $\partial v_\theta(k)/\partial\boldsymbol{\theta} = \partial\mu_\theta(k)/\partial\boldsymbol{\theta}$ for $k = 1, \ldots, K_{\text{pix}}$. The term $\alpha(k)$, $k = 1, \ldots, K_{\text{pix}}$, is known as the noise coefficient that depends on the extraneous noise sources and the detector type. In the absence of readout noise, $\alpha(k) = 1$ for all $k = 1, \ldots, K_{\text{pix}}$ [13]. In the presence of readout noise and when using a CCD camera or a Complementary Metal Oxide Semiconductor (CMOS) detector the noise coefficient is given by [12]

$$\alpha(k) := v_\theta(k)\left(\frac{e^{-v_\theta(k)}}{\sqrt{2\pi}\sigma_k}\int_{\mathbb{R}}\frac{\left(\sum_{l=1}^{\infty}\frac{v_\theta^{l-1}(k)}{(l-1)!}e^{\frac{-(z-l-\eta_k)^2}{2\sigma_k^2}}\right)^2}{\sum_{l=0}^{\infty}\frac{v_\theta^{l}(k)}{l!}e^{\frac{-(z-l-\eta_k)^2}{2\sigma_k^2}}}dz-1\right), \qquad k = 1, \ldots, K_{\text{pix}},$$

where η_k and σ_k^2 denote the mean and the variance of the readout noise at pixel C_k, respectively. The expression of the noise coefficient in the presence of readout noise and stochastic signal amplification, i.e. when using an EMCCD camera, can be found in [60].

Supposing that the object of interest is a point source and that an analytical expression is available for the PSF (e.g. the Airy profile [10] or a bivariate Gaussian profile [48] assuming a 2D case, and the Born and Wolf model [10], i.e. Eq. (2.2), assuming a 3D case), Eq. (2.3) can be used to calculate the PLAM for a single molecule microscopy experiment. However, as mentioned earlier, the lack of appropriate analytical models for PSFs and the lack of knowledge about the precise values of imaging parameters often cause major problems in the calculation of the PLAM. Additionally, it is often important to calculate the PLAM for a general experimental object as opposed to a point source. To overcome these problems, we propose an alternative approach by directly making use of an experimental image set for the calculation of the PLAM.

Other approaches are reported in the literature to address the model mismatch issue. For instance, in [61] a phase-retrieved pupil function was used to generate a more accurate model for the PSF of the optical system. This more accurate PSF model was then used for the calculation of the PLAM. In [62], a similar approach was used to model engineered

PSFs. Such techniques, however, are limited to point-like objects and depend on a variety of imaging parameters, such as the numerical aperture of the objective lens (see e.g. [61]).

2.3.2 Experimental image sets and experimental PSFs

In this section, we develop notation for an experimental image set which will be useful for our later discussions. A 3D experimental image set is a set of pixelated images of an object acquired at different defocus levels [55, 56], which are corrupted by extraneous noise sources, such as background and readout noise, during the measurement process [13]. In addition, due to the stochastic nature of light, the acquired images are also inherently stochastic [12,43]. Let $z_p \in \mathbb{R},\ p = 1, \ldots, K_{\text{stk}}$, denote the defocus level in the object space, where K_{stk} is the total number of levels. We define an acquired 3D experimental image set as a realization $\{h_{k,p} \in \mathbb{R} \mid k = 1, \ldots, K_{\text{pix}},\ p = 1, \ldots, K_{\text{stk}}\}$ of an array of independent random variables $\{\mathcal{H}_{k,p} \mid k = 1, \ldots, K_{\text{pix}},\ p = 1, \ldots, K_{\text{stk}}\}$ distributed as

$$\mathcal{H}_{k,p} \sim Poisson\left(\frac{N^c}{M^2}\int_{C_k} q_{z_0,z_p}\left(\frac{x}{M} - x_0, \frac{y}{M} - y_0\right) dxdy + b^c_{k,p}\right) * \mathcal{N}(0, \sigma_k^{2,c}), \qquad (2.4)$$

where $N^c > 0$ is the expected photon count, $*$ denotes the convolution operator, $b^c_{k,p} \geq 0$ is the background level at pixel $C_k,\ k = 1, \ldots, K_{\text{pix}}$, at defocus level $z_p,\ p = 1, \ldots, K_{\text{stk}}$, and $\mathcal{N}(0, \sigma_k^{2,c})$ denotes a zero-mean Gaussian distribution with variance $\sigma_k^{2,c}$ associated with the readout noise. If the microscope system is spatially-invariant along the z-axis, we have $q_{z_0,z_p} := q_{z_p - z_0}$. The above notation can also be used for a 2D localization problem simply by assuming $K_{\text{stk}} = 1$ and $z_p = z_0$. In this case, the experimental image set contains only a single image of the object. If the object of interest is a point source, the experimental image set pertains to an experimental PSF which can be collected by imaging a bead sample (see Section 2.2.1).

After acquiring an experimental image set, e.g. an experimental PSF, the next step is to estimate the image function q_{z_0}. Once we estimate the image function, we can substitute it into Eq. (2.1) to obtain an analytical expression for $\mu_\theta(k),\ k = 1, \ldots, K_{\text{pix}}$, which can then be used to analytically calculate the partial derivatives required in the FIM equation

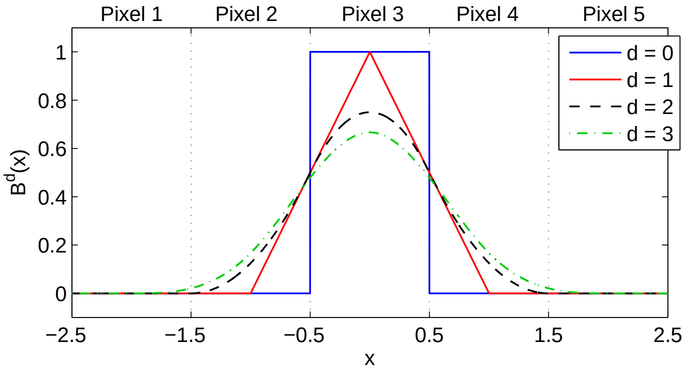

Figure 2.1: A plot of the symmetrical B-splines. Symmetrical B-splines of degree d for $d = 0, 1, 2, 3$, with unit element spacing, lead to nearest neighborhood, linear, quadratic and cubic interpolation of the experimental image set, respectively. The vertical dotted lines show the pixel boundaries and the B-splines are located at the center of pixel 3. Reprinted with permission from [34].

(i.e. Eq. (2.3)). This will be the topic of subsequent sections.

2.3.3 Piecewise polynomial fitting

Splines are piecewise polynomials with pieces that are smoothly connected together [49]. They have been extensively used in multidimensional data fitting (e.g. surface fitting) and interpolation problems due to their useful properties [38, 50]. One of the important characteristics of a spline is that it can be represented in the form of a linear combination of basis functions known as B-splines [38]. B-splines have a number of important properties, namely affine invariance, local support and positivity [51], which make them of interest for our application. We therefore take advantage of splines to estimate the image function. In particular, we next explain how to fit a volume spline to a 3D experimental image set. Fitting a surface spline to a 2D experimental image set is a special case of the 3D fitting by simply setting $K_{\text{stk}} = 1$ and $z_p = z_0$.

Denote by $\Delta x > 0$, and $\Delta y > 0$, the physical pixel size in the image space in the x and y directions, respectively. Let $\Delta x_0 := \Delta x/M$, and $\Delta y_0 := \Delta y/M$, be the effective pixel size in the object space in the x and y directions, respectively, where M is the lateral magnification of the microscope optics. Let $\Delta z_0 > 0$ be the step size in the z-direction in the object space. A volume spline of degree $d \in \mathbb{N}_0$ with element spacing $(\Delta x_0, \Delta y_0, \Delta z_0)$ in the object space is given by [51]

$$s_a^d(x,y,z) := \sum_{m=1}^{K_{\text{row}}} \sum_{n=1}^{K_{\text{col}}} \sum_{p=1}^{K_{\text{stk}}} a_{m,n,p} \beta^d \left(\frac{x}{\Delta x_0} - n \right) \beta^d \left(\frac{y}{\Delta y_0} - m \right) \beta^d \left(\frac{z}{\Delta z_0} - p \right), \tag{2.5}$$

where $(x,y,z) \in \mathbb{R}^3$, $\{a_{m,n,p} \mid m = 1,\ldots,K_{\text{row}},\ n = 1,\ldots,K_{\text{col}},\ p = 1,\ldots,K_{\text{stk}}\}$ are called the B-spline coefficients, K_{row} and K_{col} denote the number of rows and columns of the image, respectively, such that $K_{\text{row}} \times K_{\text{col}} = K_{\text{pix}}$, K_{stk} denotes the total number of defocus levels, and β^d denotes the symmetrical B-spline of degree d given by (see Fig. 2.1)

$$\beta^d(x) := \sum_{i=0}^{d+1} \frac{(-1)^i}{d!} \binom{d+1}{i} \left(x + \frac{d+1}{2} - i \right)^d u \left(x + \frac{d+1}{2} - i \right), \qquad x \in \mathbb{R}, \tag{2.6}$$

where

$$u(x) = \begin{cases} 1, & x \geq 0 \\ 0, & x < 0 \end{cases} .$$

Given the noisy measurements $h_{k,p}$ at pixels $C_k,\ k = 1,\ldots,K_{\text{pix}}$, and at defocus levels $z_p,\ p = 1,\ldots,K_{\text{stk}}$, our problem is to find a volume spline $s_a^d(x,y,z)$ for $(x,y,z) \in \mathbb{R}^3$, such that

$$\int_{C_k} s_a^d \left(\frac{x}{M} - x_0, \frac{y}{M} - y_0, z_p - z_0 \right) dxdy \approx h_{k,p} - b_{k,p}^c, \quad k = 1,\ldots,K_{\text{pix}}, p = 1,\ldots,K_{\text{stk}}, \tag{2.7}$$

where $b_{k,p}^c$ denotes the background level at pixel C_k and at defocus level z_p, and is assumed to be known or can be estimated [26]. It is important to note that the above problem is an interpolation problem with the exception that, for each defocus level z_p, the data points are calculated by integrating the continuous surface spline over the pixels instead of evaluating it at the centers of the pixels/intervals (see e.g. [38, 52]). This integral sampling is the appropriate way of modeling the photon detection process in fluorescence microscopy

[12, 13, 43]. Our problem is, in fact, to find a set of B-spline coefficients that minimizes the cost function

$$\sum_{k=1}^{K_{\text{pix}}} \sum_{p=1}^{K_{\text{stk}}} \left| \int_{C_k} s_a^d \left(\frac{x}{M} - x_0, \frac{y}{M} - y_0, z_p - z_0 \right) dxdy - (h_{k,p} - b_{k,p}^c) \right|^2 .$$

To introduce a concise matrix notation for the above cost function we define

$$\boldsymbol{h} := \left(h_{1,1} - b_{1,1}^c, \ldots, h_{K_{\text{pix}},1} - b_{K_{\text{pix}},1}^c, h_{1,2} - b_{1,2}^c, \ldots, h_{K_{\text{pix}},K_{\text{stk}}} - b_{K_{\text{pix}},K_{\text{stk}}}^c \right)^T \in \mathbb{R}^K,$$

and

$$\boldsymbol{a} := (a_{1,1,1}, \ldots, a_{K_{\text{row}},1,1}, a_{1,2,1}, \ldots, a_{K_{\text{row}},K_{\text{col}},1}, a_{1,1,2}, \ldots, a_{K_{\text{row}},K_{\text{col}},K_{\text{stk}}})^T \in \mathbb{R}^K,$$

where $K := K_{\text{pix}} \times K_{\text{stk}}$ is the total number of data points. We also define $\boldsymbol{S} \in \mathbb{R}^{K \times K}$ such that

$$\begin{gathered} \boldsymbol{S}_{k+(i-1)K_{\text{pix}}, m+(n-1)K_{\text{row}}+(p-1)K_{\text{pix}}} = \\ \int_{C_k} \beta^d \left(\frac{\frac{x}{M} - x_0}{\Delta x_0} - n \right) \beta^d \left(\frac{\frac{y}{M} - y_0}{\Delta y_0} - m \right) d\boldsymbol{r} \beta^d \left(\frac{z_i - z_0}{\Delta z_0} - p \right), \quad k = 1, \ldots, K_{\text{pix}}, \\ i, p = 1, \ldots, K_{\text{stk}},\ m = 1, \ldots, K_{\text{row}},\ n = 1, \ldots, K_{\text{col}}, \end{gathered}$$

where $\boldsymbol{r} = (x, y) \in \mathbb{R}^2$. Using this matrix notation the cost function is given by

$$\epsilon(\boldsymbol{a}) := \|\boldsymbol{h} - \boldsymbol{S}\boldsymbol{a}\|^2, \qquad \boldsymbol{a} \in \mathbb{R}^K, \tag{2.8}$$

where $\| \cdot \|$ denotes the Euclidean (ℓ_2) norm.

Minimizing the cost function in Eq. (2.8) leads to an exact spline fit for the experimental image set (i.e. zero error for the cost function). However, in practice and as described in Section 2.3.2, experimental image sets are inherently stochastic and are typically corrupted by extraneous noise. As such, an exact spline fit does not necessarily provide the best continuous approximation. Hence, we regularize the optimization problem using an additional term that intends to suppress the noise [38, 52]

$$\phi_l^d(\boldsymbol{a}) := \int_{\mathbb{R}^3} \|\boldsymbol{D}^l s_a^d(x,y,z)\|^2 dxdydz, \qquad \boldsymbol{a} \in \mathbb{R}^K,\ d \in \mathbb{N}_0,\ l \leq d, \tag{2.9}$$

where $\boldsymbol{D}^l$ is the vector of all possible partial derivatives of order l. For instance, for $l = 1$ we have

$$\phi_1^d(\boldsymbol{a}) = \int_{\mathbb{R}^3} \left[\left(\frac{\partial s_a^d(x,y,z)}{\partial x} \right)^2 + \left(\frac{\partial s_a^d(x,y,z)}{\partial y} \right)^2 + \left(\frac{\partial s_a^d(x,y,z)}{\partial z} \right)^2 \right] dxdydz, \quad \boldsymbol{a} \in \mathbb{R}^K.$$

We next express the regularization cost function, i.e. Eq. (2.9), in terms of the expansion of the B-spline coefficients. This will help to introduce a matrix notation for the regularization term. Substituting Eq. (2.5) into Eq. (2.9) yields

$$\begin{aligned}
\phi_l^d(\boldsymbol{a}) &= \int_{\mathbb{R}^3} \|\boldsymbol{D}^l s_a^d(x,y,z)\|^2 dxdydz = \sum_{q_1+q_2+q_3=l} \binom{l}{q_1, q_2, q_3} \int_{\mathbb{R}^3} \left(\frac{\partial^l s_a^d(x,y,z)}{\partial x^{q_1} \partial y^{q_2} \partial z^{q_3}} \right)^2 dxdydz \\
&= \sum_{q_1+q_2+q_3=l} \binom{l}{q_1, q_2, q_3} \int_{\mathbb{R}^3} \left(\frac{\partial^l}{\partial x^{q_1} \partial y^{q_2} \partial z^{q_3}} \sum_{m,n,p} a_{m,n,p} \right. \\
&\qquad \left. \times\ \beta^d\left(\frac{x}{\Delta x_0} - n\right) \beta^d\left(\frac{y}{\Delta y_0} - m\right) \beta^d\left(\frac{z}{\Delta z_0} - p\right) \right)^2 dxdydz \\
&= \sum_{q_1+q_2+q_3=l} \binom{l}{q_1, q_2, q_3} \int_{\mathbb{R}^3} \left(\sum_{m,n,p} a_{m,n,p} \right. \\
&\qquad \left. \times\ \frac{\partial^{q_1}}{\partial x^{q_1}} \beta^d\left(\frac{x}{\Delta x_0} - n\right) \frac{\partial^{q_2}}{\partial y^{q_2}} \beta^d\left(\frac{y}{\Delta y_0} - m\right) \frac{\partial^{q_3}}{\partial z^{q_3}} \beta^d\left(\frac{z}{\Delta z_0} - p\right) \right)^2 dxdydz,
\end{aligned}$$

for $\boldsymbol{a} \in \mathbb{R}^K$, where $\sum_{m,n,p} := \sum_{m=1}^{K_{\text{row}}} \sum_{n=1}^{K_{\text{col}}} \sum_{p=1}^{K_{\text{stk}}}$. With a little manipulation, it follows

$$\begin{aligned}
\phi_l^d(\boldsymbol{a}) &= \sum_{q_1+q_2+q_3=l} \binom{l}{q_1, q_2, q_3} \int_{\mathbb{R}^3} \\
&\left(\sum_{m,n,p} a_{m,n,p} \frac{\partial^{q_1}}{\partial x^{q_1}} \beta^d\left(\frac{x}{\Delta x_0} - n\right) \frac{\partial^{q_2}}{\partial y^{q_2}} \beta^d\left(\frac{y}{\Delta y_0} - m\right) \frac{\partial^{q_3}}{\partial z^{q_3}} \beta^d\left(\frac{z}{\Delta z_0} - p\right) \right) \times \\
&\left(\sum_{m',n',p'} a_{m',n',p'} \frac{\partial^{q_1}}{\partial x^{q_1}} \beta^d\left(\frac{x}{\Delta x_0} - n'\right) \frac{\partial^{q_2}}{\partial y^{q_2}} \beta^d\left(\frac{y}{\Delta y_0} - m'\right) \frac{\partial^{q_3}}{\partial z^{q_3}} \beta^d\left(\frac{z}{\Delta z_0} - p'\right) \right) dxdydz.
\end{aligned}$$

Rearranging the above equation, it follows

$$\phi_l^d(\boldsymbol{a}) = \sum_{m,m'=1}^{K_{\text{row}}} \sum_{n,n'=1}^{K_{\text{col}}} \sum_{p,p'=1}^{K_{\text{stk}}} a_{m,n,p} a_{m',n',p'} \times \sum_{q_1+q_2+q_3=l} \binom{l}{q_1, q_2, q_3} B_{\Delta x_0}^{q_1}(n,n') B_{\Delta y_0}^{q_2}(m,m') B_{\Delta z_0}^{q_3}(p,p'), \qquad \boldsymbol{a} \in \mathbb{R}^K, \tag{2.10}$$

where

$$B_\Delta^q(n,n') := \int_{\mathbb{R}} \frac{\partial^q}{\partial t^q} \beta^d\left(\frac{t}{\Delta} - n\right) \frac{\partial^q}{\partial t^q} \beta^d\left(\frac{t}{\Delta} - n'\right) dt, \quad n, n' \in \mathbb{N},\ q = 1, \ldots, l,\ \Delta > 0.$$

We now define $\boldsymbol{B} \in \mathbb{R}^{K \times K}$ such that for $m, m' = 1, \ldots, K_{\text{row}},\ n, n' = 1, \ldots, K_{\text{col}},\ p, p' = 1, \ldots, K_{\text{stk}}$,

$$\boldsymbol{B}_{(p-1)K_{\text{pix}}+(n-1)K_{\text{row}}+m,(p'-1)K_{\text{pix}}+(n'-1)K_{\text{row}}+m'} = \sum_{q_1+q_2+q_3=l} \binom{l}{q_1, q_2, q_3} B_{\Delta x_0}^{q_1}(n,n') B_{\Delta y_0}^{q_2}(m,m') B_{\Delta z_0}^{q_3}(p,p').$$

Using this notation, Eq. (2.10) can be expressed in matrix form as follows (see also [52])

$$\phi(\boldsymbol{a}) = \boldsymbol{a}^T \boldsymbol{B} \boldsymbol{a}, \qquad \boldsymbol{a} \in \mathbb{R}^K,$$

where for conciseness the superscript d and subscript l are dropped.

To estimate the B-spline coefficients in the presence of stochasticity and noise, by making use of the matrix notation introduced above, we solve the following optimization problem

$$\hat{\boldsymbol{a}} = \underset{\boldsymbol{a} \in \mathbb{R}^K}{\operatorname{argmin}} \left(\epsilon(\boldsymbol{a}) + \gamma \phi(\boldsymbol{a})\right) = \underset{\boldsymbol{a} \in \mathbb{R}^K}{\operatorname{argmin}} \left(\|\boldsymbol{h} - \boldsymbol{S}\boldsymbol{a}\|^2 + \gamma \boldsymbol{a}^T \boldsymbol{B} \boldsymbol{a}\right), \tag{2.11}$$

which is a regularized least-squares problem [38, 49]. The first term measures the error between the data and the model in the least squares sense whereas the second term imposes a smoothness constraint on the solution. The regularization (smoothing) factor $\gamma \geq 0$

controls the trade-off between fidelity to the data and the smoothness of the estimate. Using vector differentiation [52], it is easy to verify that the minimizer to Eq. (2.11) is given by the solution of the following equation

$$\left(\boldsymbol{S}^T\boldsymbol{S} + \gamma\boldsymbol{B}\right)\hat{\boldsymbol{a}} = \boldsymbol{S}^T\boldsymbol{h}, \tag{2.12}$$

which can be solved efficiently using Gaussian elimination or singular value decomposition.

We note that the solution of the above equation can be derived given a specific choice of the smoothing factor γ, the derivative order l and the B-spline degree d. The smoothing factor can be chosen based on a priori information, e.g. the variance of the measurement noise. By setting $\gamma = 0$, the optimization problem in Eq. (2.11) reduces to a standard least squares problem [38]. The typical choice for the derivative order in modern statistics literature is $l = 2$, although other orders can also be easily used [50]. Given the order of derivatives, an appropriate degree for the B-splines can be chosen as $d = 2l - 1$ [38]. The rationale for this choice is Schoenberg's work [51] in which it is demonstrated for a 1D problem that the solution that minimizes the error in Eq. (2.11) is a spline of degree $d = 2l - 1$ with simple knots at the data points and some natural end conditions. For instance, cubic spline interpolation (i.e. using a spline of degree $d = 3$) is the appropriate choice when using the derivatives of order $l = 2$.

2.3.4 Calculation of the Fisher information matrix

Once we estimate the B-spline coefficients $\hat{\boldsymbol{a}}$ through Eq. (2.12), we can substitute them into Eq. (2.5) and find the spline fit to the experimental image set $\boldsymbol{h}$. This volume fit $\hat{s}_a^d$ after normalization can be used to obtain an estimate of the image function. For conciseness, define $\sum_{m,n,p} := \sum_{m=1}^{K_{\mathrm{row}}} \sum_{n=1}^{K_{\mathrm{col}}} \sum_{p=1}^{K_{\mathrm{stk}}}$. We define the normalization factor

$$\begin{aligned} C(z_0) : &= \int_{\mathbb{R}^2} \hat{s}_a^d(x, y, z_0) d\boldsymbol{r} \\ &= \sum_{m,n,p} \hat{a}_{m,n,p} \int_{\mathbb{R}^2} \beta^d \left(\frac{x}{\Delta x_0} - n \right) \beta^d \left(\frac{y}{\Delta y_0} - m \right) d\boldsymbol{r} \beta^d \left(\frac{z_0}{\Delta z_0} - p \right) \\ &= \Delta x_0 \Delta y_0 \sum_{m,n,p} \hat{a}_{m,n,p} \beta^d \left(\frac{z_0}{\Delta z_0} - p \right), \qquad z_0 \in \mathbb{R}, \end{aligned} \tag{2.13}$$

where $\boldsymbol{r} = (x, y) \in \mathbb{R}^2$ and we applied the B-spline property $\int_{\mathbb{R}} \beta^d(x) dx = 1$ for $d \in \mathbb{N}_0$ (see Appendix A for details). The estimated image function is given by

$$\hat{q}_{z_0}(x, y) := \frac{\hat{s}_a^d(x, y, z_0)}{C(z_0)} = \sum_{m,n,p} \tilde{a}_{m,n,p}^{z_0} \beta^d \left(\frac{x}{\Delta x_0} - n \right) \beta^d \left(\frac{y}{\Delta y_0} - m \right) \beta^d \left(\frac{z_0}{\Delta z_0} - p \right),$$

where $(x, y) \in \mathbb{R}^2$, and $\tilde{a}_{m,n,p}^{z_0} := \hat{a}_{m,n,p} / C(z_0)$, $m = 1, \ldots, K_{\mathrm{row}}$, $n = 1, \ldots, K_{\mathrm{col}}$, $p = 1, \ldots, K_{\mathrm{stk}}$, are termed the normalized B-spline coefficients.

We now have an estimate of the image function that can be used to calculate the PLAM. Substituting the estimated image function into Eq. (2.1), for $k = 1, \ldots, K_{\mathrm{pix}}$, we have

$$\begin{aligned} \mu_\theta(k) &\approx \frac{N}{M^2} \int_{C_k} \hat{q}_{z_0} \left(\frac{x}{M} - x_0, \frac{y}{M} - y_0 \right) d\boldsymbol{r} \\ &= \frac{N}{M^2} \sum_{m,n,p} \tilde{a}_{m,n,p}^{z_0} \int_{C_k} \beta^d \left(\frac{\frac{x}{M} - x_0}{\Delta x_0} - n \right) \beta^d \left(\frac{\frac{y}{M} - y_0}{\Delta y_0} - m \right) d\boldsymbol{r} \beta^d \left(\frac{z_0}{\Delta z_0} - p \right). \end{aligned} \tag{2.14}$$

It is important to note that, assuming that the pixel size, the magnification and the location of the object are unchanged, the integral in the above expression is constant and therefore it can be precalculated once and used in different experiments.

The next step is to calculate the partial derivatives of $\mu_\theta(k)$ w.r.t. the unknown parameters. An interesting feature of B-splines is that their first derivatives can be obtained analytically through the following expression [49]

$$\frac{\partial \beta^d(x)}{\partial x} = \beta^{d-1}(x + \frac{1}{2}) - \beta^{d-1}(x - \frac{1}{2}), \qquad x \in \mathbb{R},\ d \in \mathbb{N}. \tag{2.15}$$

Using this identity and taking the partial derivatives of both sides of Eq. (2.14) w.r.t. x_0 for $k = 1, \dots, K_{\text{pix}}$, we have (for details see Appendix B)

$$\begin{aligned}\frac{\partial \mu_\theta(k)}{\partial x_0} \approx \frac{-N}{M^2} \sum_{m=1}^{K_{\text{row}}} \sum_{n=1}^{K_{\text{col}}+1} \sum_{p=1}^{K_{\text{stk}}} \frac{\tilde{a}^{z_0}_{m,n,p} - \tilde{a}^{z_0}_{m,n-1,p}}{\Delta x_0} \beta^d \left(\frac{z_0}{\Delta z_0} - p \right) \\ \times \int_{C_k} \beta^{d-1} \left(\frac{\frac{x}{M} - x_0}{\Delta x_0} - n + \frac{1}{2} \right) \beta^d \left(\frac{\frac{y}{M} - y_0}{\Delta y_0} - m \right) d\boldsymbol{r},\end{aligned}$$

where $\boldsymbol{r} = (x, y) \in \mathbb{R}^2$ and we assumed $\tilde{a}^{z_0}_{m,0,p} = \tilde{a}^{z_0}_{m,K_{\text{col}}+1,p} = 0$, $m = 1, \dots, K_{\text{row}}$, $p = 1, \dots, K_{\text{stk}}$. Similarly, we can obtain the partial derivatives w.r.t. y_0 for $k = 1, \dots, K_{\text{pix}}$, as follows

$$\begin{aligned}\frac{\partial \mu_\theta(k)}{\partial y_0} \approx \frac{-N}{M^2} \sum_{m=1}^{K_{\text{row}}+1} \sum_{n=1}^{K_{\text{col}}} \sum_{p=1}^{K_{\text{stk}}} \frac{\tilde{a}^{z_0}_{m,n,p} - \tilde{a}^{z_0}_{m-1,n,p}}{\Delta y_0} \beta^d \left(\frac{z_0}{\Delta z_0} - p \right) \\ \times \int_{C_k} \beta^{d} \left(\frac{\frac{x}{M} - x_0}{\Delta x_0} - n \right) \beta^{d-1} \left(\frac{\frac{y}{M} - y_0}{\Delta y_0} - m + \frac{1}{2} \right) d\boldsymbol{r},\end{aligned}$$

where $\tilde{a}^{z_0}_{0,n,p} = \tilde{a}^{z_0}_{K_{\text{row}}+1,n,p} = 0$, for all $n = 1, \dots, K_{\text{col}}$, and $p = 1, \dots, K_{\text{stk}}$. We can also derive the partial derivatives w.r.t. z_0 for $k = 1, \dots, K_{\text{pix}}$, as follows (see Appendix B)

$$\begin{aligned}\frac{\partial \mu_\theta(k)}{\partial z_0} \approx \frac{N}{M^2} \sum_{m=1}^{K_{\text{row}}} \sum_{n=1}^{K_{\text{col}}} \sum_{p=1}^{K_{\text{stk}}+1} \frac{\tilde{a}^{z_0}_{m,n,p} - \tilde{a}^{z_0}_{m,n,p-1}}{\Delta z_0} \beta^{d-1} \left(\frac{z_0}{\Delta z_0} - p + \frac{1}{2} \right) \\ \times \int_{C_k} \beta^{d} \left(\frac{\frac{x}{M} - x_0}{\Delta x_0} - n \right) \beta^{d} \left(\frac{\frac{y}{M} - y_0}{\Delta y_0} - m \right) d\boldsymbol{r} - \mu_\theta(k) \xi(z_0),\end{aligned} \tag{2.16}$$

where $\tilde{a}^{z_0}_{m,n,0} = \tilde{a}^{z_0}_{m,n,K_{\text{stk}}+1} = 0$, for all $m = 1, \dots, K_{\text{row}}$, and $n = 1, \dots, K_{\text{col}}$, and for $z_0 \in \mathbb{R}$,

$$\xi(z_0) := \frac{1}{C(z_0)} \frac{\partial C(z_0)}{\partial z_0} = \frac{\Delta x_0 \Delta y_0}{\Delta z_0} \sum_{m=1}^{K_{\text{row}}} \sum_{n=1}^{K_{\text{col}}} \sum_{p=1}^{K_{\text{stk}}+1} (\tilde{a}^{z_0}_{m,n,p} - \tilde{a}^{z_0}_{m,n,p-1}) \beta^{d-1} \left(\frac{z_0}{\Delta z_0} - p + \frac{1}{2} \right).$$

We now have estimates of the partial derivatives of $\mu_\theta(k)$, $k = 1, \ldots, K_{\text{pix}}$, w.r.t. the parameter vector of interest. This allows to determine the PLAM for a fluorescence microscopy setup directly from an experimental image set.

2.3.5 Limit of the accuracy for estimating other parameters

In the previous section, we were primarily concerned with the calculation of the best possible localization accuracy directly from an experimental image set. However, using the general statistical framework described in Section 2.3.1 we can also calculate the best possible accuracy with which other parameters can be estimated, such as the photon count and the background level. To this end, we simply define an extended parameter vector $\boldsymbol{\theta} := (x_0, y_0, z_0, N, b) \in \Theta \subseteq \mathbb{R}^5$, where $b := b_k$, $k = 1, \ldots, K_{\text{pix}}$, denotes the constant background level. Since the photon count is independent of the estimated image function, from Eq. (2.14) it is straightforward to verify that

$$\frac{\partial v_\theta(k)}{\partial N} = \frac{\partial}{\partial N}(\mu_\theta(k) + b) = \frac{\mu_\theta(k)}{N}, \qquad k = 1, \ldots, K_{\text{pix}}.$$

Similarly, for the background level we have

$$\frac{\partial v_\theta(k)}{\partial b} = \frac{\partial}{\partial b}(\mu_\theta(k) + b) = 1, \qquad k = 1, \ldots, K_{\text{pix}}.$$

By substituting the above equations into Eq. (2.3), we can obtain the best possible accuracy for estimating the photon count and the background level.

2.4 Results and discussion

2.4.1 Verification of the approach in the absence of noise

We have developed an approach for the calculation of the best possible accuracy with which a general object can be localized, i.e. the PLAM, directly from 2D and 3D experimental image sets. We defer to Sections 2.4.4 and 2.4.5 examples concerning the PLAM for general experimental objects. Here we primarily focus on point-like objects (e.g. a single molecule) and, as such, the experimental image set pertains to an experimental

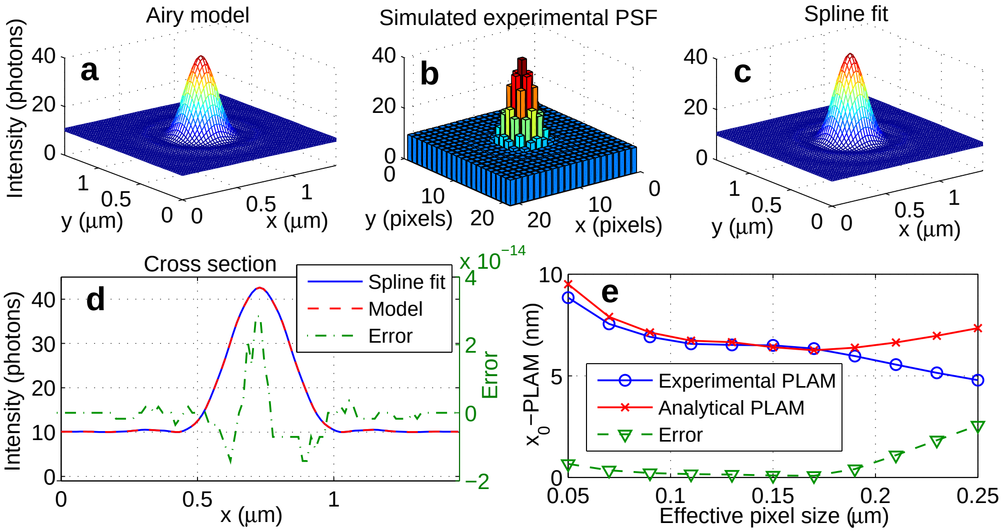

Figure 2.2: Verification of the approach in idealized imaging conditions for a 2D PSF. (a) The image of a point source simulated using the Airy profile for a 100x, NA 1.4 objective lens with an emission wavelength of 690 nm. (b) An experimental PSF simulated using the model image in (a) in the absence of stochasticity and noise. The pixel size and the detector size are 7 μm × 7 μm and 21 × 21 pixels, respectively. (c) The bicubic spline fit of the simulated experimental PSF in (b). (d) The line profiles that pass through the peaks of the analytical PSF and the spline fit, and the error between the line profiles. (e) The deduced experimental x_0-PLAM and its corresponding analytical PLAM as a function of the effective pixel size in the object space (the results for y_0-PLAM are similar due to the radial symmetry of the PSF and are omitted). The absolute difference error is also shown. For the calculation of the PLAM, we assumed a background level of $b = 10$ photons/pixel and a photon count of $N = 500$ photons. Reprinted with permission from [34].

PSF. We refer to the PLAM deduced from an experimental PSF using the aforementioned approach as the experimental PLAM, whereas the PLAM calculated from an analytical PSF is referred to as the analytical PLAM. We further refer to the limit of the localization accuracy for the x, y and z coordinates of the single molecule as x_0-PLAM, y_0-PLAM and z_0-PLAM, respectively. For a 2D PSF, the z_0-PLAM is not relevant. It is important to verify the performance of the developed approach in terms of the deviation of the experimental PLAM from the analytical PLAM for a simulated experimental PSF in idealized imaging conditions. We dedicate this section to this verification.

In particular, we assume idealized imaging conditions where the experimental PSF is devoid of stochasticity, due to the photon statistics, and extraneous noise, such as Poisson-distributed background noise and Gaussian-distributed readout noise. Considering these conditions, we simulate 2D and 3D experimental PSFs using analytical PSFs, such as the Airy PSF model and the Born and Wolf PSF model, respectively [10]. We then calculate the experimental PLAM using the proposed approach given the simulated experimental PSFs. We investigate the performance of our approach by comparing the results in two different steps. The first step concerns the comparison of the image profiles of the spline fit to the simulated experimental PSF and its associated analytical model. The second step compares the deduced experimental PLAM with its corresponding analytical PLAM.

We first study a 2D case. Figs. 2.2(a) and 2.2(b) show the simulated model image of an in-focus point source, i.e. the Airy profile [10], which is used as the 2D analytical PSF model, and the simulated 2D experimental PSF using this model, respectively. A bicubic spline is then fit to the simulated experimental PSF (see Fig. 2.2(c)). A Comparison of the cross sections of the fit and the analytical PSF suggests that in idealized imaging conditions the spline fit provides an appropriate estimate of the image function (see Fig. 2.2(d), the (absolute difference) error is consistently less than 4×10^{-14} photons/pixel). We next compare the deduced experimental PLAM with its corresponding analytical PLAM. In idealized imaging conditions, altering the effective pixel size, i.e. the physical pixel size divided by the lateral magnification, can potentially vary the deduced PLAM since it changes the spatial sampling of the PSF. Therefore, we calculate the experimental and analytical PLAMs as functions of the effective pixel size in Fig. 2.2(e). For effective pixel sizes ranging from 0.05 μm to 0.2 μm, the experimental x_0-PLAM is very close to the analytical x_0-PLAM. For this range the absolute difference error is consistently below 0.6 nm (i.e. the relative error is below 7 %). However, as the effective pixel size increases beyond 0.2 μm, the experimental x_0-PLAM deviates from the analytical x_0-PLAM. For example, the relative error for the effective pixel size of 0.25 μm is approximately 35 %. This result is not surprising considering the fact that a large effective pixel size implies a coarser spatial sampling of the analytical PSF which, in turn, leads to a less accurate

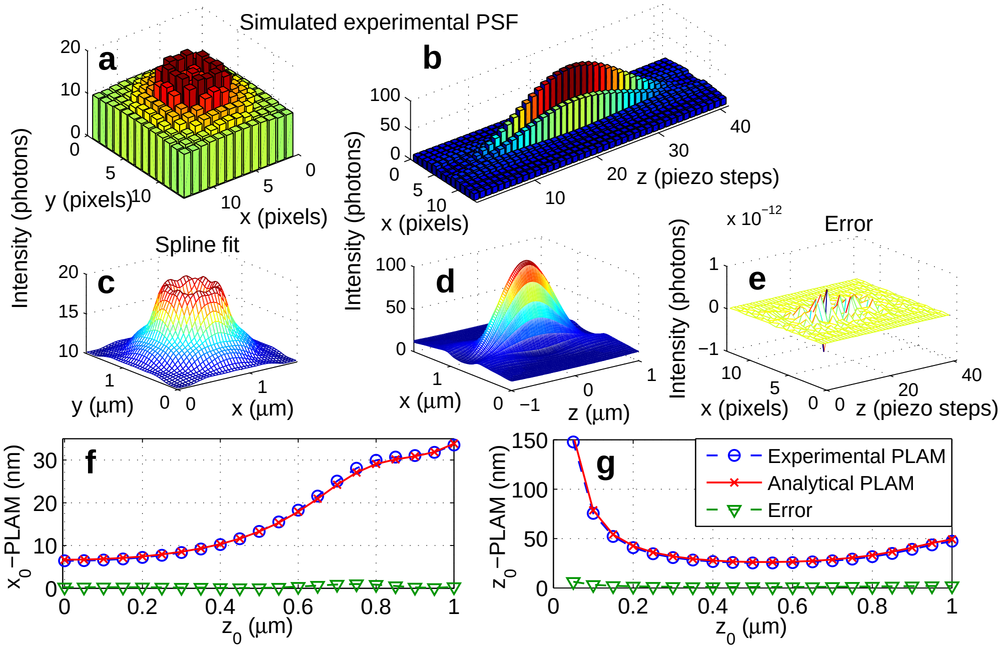

Figure 2.3: Verification of the approach in idealized imaging conditions for a 3D PSF. (a), (b) xy- (at $z_0 = 0.8$ μm) and xz-projections of an experimental PSF simulated using the Born and Wolf 3D PSF model for a 100x, NA 1.4 objective lens and an emission wavelength of 690 nm in the absence of stochasticity and noise. The refractive index of the immersion oil n_{oil} is set to 1.515. The pixel size, the z-step size and the detector size are 13 μm × 13 μm, 50 nm and 13 × 13 pixels, respectively. (c), (d) xy and xz projections of the cubic volume spline fit of the simulated experimental PSF. (e) The error between the analytical PSF and the spline fit evaluated at the pixels and at the z-steps. (f) The deduced experimental x_0-PLAM and its corresponding analytical PLAM as a function of the z_0 position of the single molecule in the object space (the results for y_0-PLAM are similar and are omitted). The error is also shown. (g) The deduced experimental z_0-PLAM and its corresponding analytical PLAM as a function of z_0, and the error between them. For the calculation of the PLAM, we assumed a background level of $b = 10$ photons/pixel and a photon count of $N = 500$ photons. Reprinted with permission from [34].

spline fit. We note that effective pixel sizes beyond 0.2 μm, however, are rare in practice.

For the verification of the 3D case, an experimental PSF is simulated using the Born and Wolf analytical 3D PSF model [10] (see Figs. 2.3(a) and 2.3(b) for xy- and xz-projections). A cubic volume spline is then fit to the simulated 3D experimental PSF (see Figs. 2.3(c) and 2.3(d) for xy and xz projections). The negligible error between the spline fit and the analytical PSF, evaluated at the pixels and at the z-steps, suggests that in idealized imaging conditions the spline fit provides an accurate estimate of the image function (see Fig. 2.3(e) for the xz projection of the error, where the absolute error is consistently less than 10^{-12} photons/pixel/z-step). We next compare the deduced experimental PLAM with its corresponding analytical PLAM as a function of the z_0 position of the single molecule on the optical axis. This is of significant practical importance as it allows us to verify whether the deduced experimental PLAM remains valid as the single molecule moves along the z-axis. Fig. 2.3(f) shows the deduced experimental x_0-PLAM, its corresponding analytical x_0-PLAM and the absolute deviation error over the z-range of [0, 1] μm (since the PLAMs are axially symmetric, the results for the z-range of [-1, 0] μm are omitted). The error is consistently smaller than 0.9 nm over the z-range of [-1, 1] μm and the average percentage error over this range is approximately 2 %. Similar results are observed for the deduced experimental z_0-PLAM (see Fig. 2.3(g)), where the error is consistently smaller than 4.3 % over the z-range of [-1, 1] μm, with an average of 3.9 %. We would like to note that these results are for a pixel size of 13 μm × 13 μm and that the error can be further decreased by decreasing the pixel size.

2.4.2 Effects of stochasticity and noise in the experimental PSF on the deduced PLAM

In practice, experimental PSFs are inherently stochastic, due to the Poisson distribution of the collected photons, and are typically corrupted by extraneous noise [13,54,56]. Hence, in this section we investigate the effects of stochasticity and noise in the experimental PSF on the deduced experimental PLAM. Figs. 2.4(a), 2.4(a') and 2.4(b), 2.4(b') show an out of focus xy-projection of the Born and Wolf 3D PSF model [10], and the corresponding xy-projection of a simulated 3D experimental PSF using this model, respectively. For the simulation of the experimental PSF, we considered both the stochasticity of the signal and the extraneous noise sources. As mentioned earlier, in the presence of noise, an exact spline fit is not appropriate. Therefore, we fit a volume cubic smoothing spline, with a small smoothing factor $\gamma = 0.01$, to the simulated experimental PSF (see Figs. 2.4(c) and 2.4(c')). Comparing the error between the simulated experimental PSF and the analytical PSF model (Fig. 2.4(d)) and between the spline fit and the analytical PSF model (Fig.

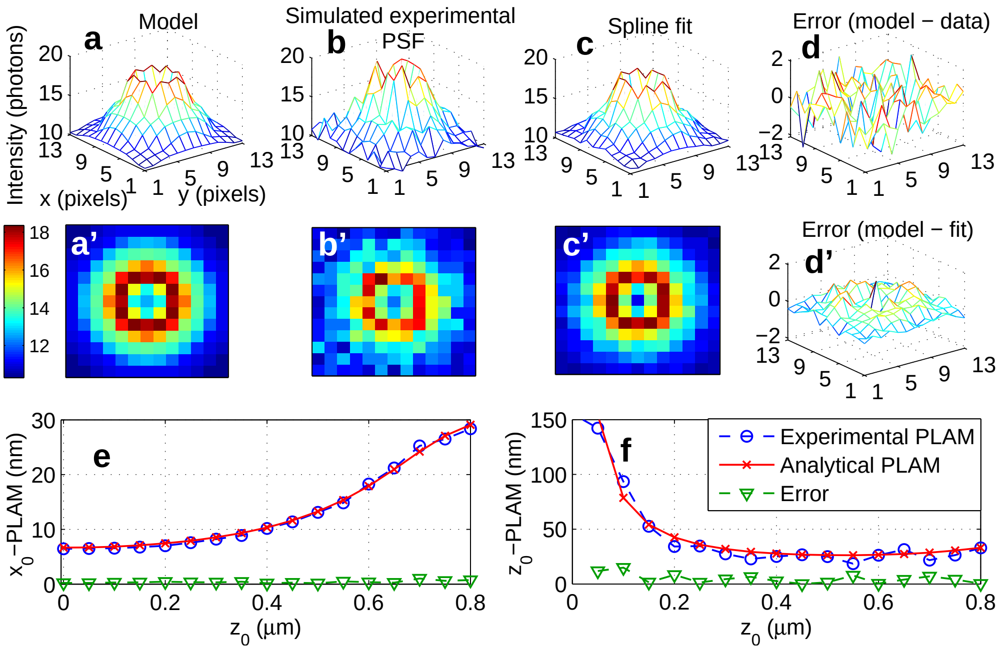

Figure 2.4: The performance of the approach in the presence of stochasticity and noise. (a), (a') An xy-projection (at $z_0 = 0.9\ \mu$m) of the Born and Wolf 3D PSF model for a 100x, NA 1.4 objective lens and an emission wavelength of 690 nm. The refractive index of the immersion oil n_{oil} is set to 1.515. (b), (b') The corresponding xy-projection of the experimental PSF simulated using the model in panels (a) and (a') in the presence of stochasticity and noise, where the standard deviation σ^c is 10 e$^-$/pixel and the photon count N^c is 10000 photons. The pixel size, the z-step size and the detector size are the same as those in Fig. 2.3. (c), (c') The xy-projection of the cubic volume spline fit of the simulated experimental PSF, where the smoothing factor γ is set to 0.01. (d), (d') The error between xy-projections of the analytical PSF model and the simulated experimental PSF (i.e. data) and between the analytical PSF model and the spline fit, respectively, evaluated at the pixels. (e), (f) The deduced experimental x_0-PLAM and z_0-PLAM and their corresponding analytical PLAMs as functions of the z_0 position of the single molecule in the object space. The errors are also shown. For the calculation of the PLAM, we assumed a background level of $b = 10$ photons/pixel and a photon count of $N = 500$ photons. Reprinted with permission from [34].

2.4(d')), evaluated at the pixels, suggests that the smoothing spline fitting can suppress the stochasticity and noise (the error range is reduced from [-2, 2] photons/pixel in Fig. 2.4(d) to [-1, 1] photon/pixel in Fig. 2.4(d')). This can also be obviously observed in Fig. 2.4(c'), which shows a similar pattern to Fig. 2.4(a').

Fig. 2.4(e) shows the deduced experimental x_0-PLAM, its corresponding analytical

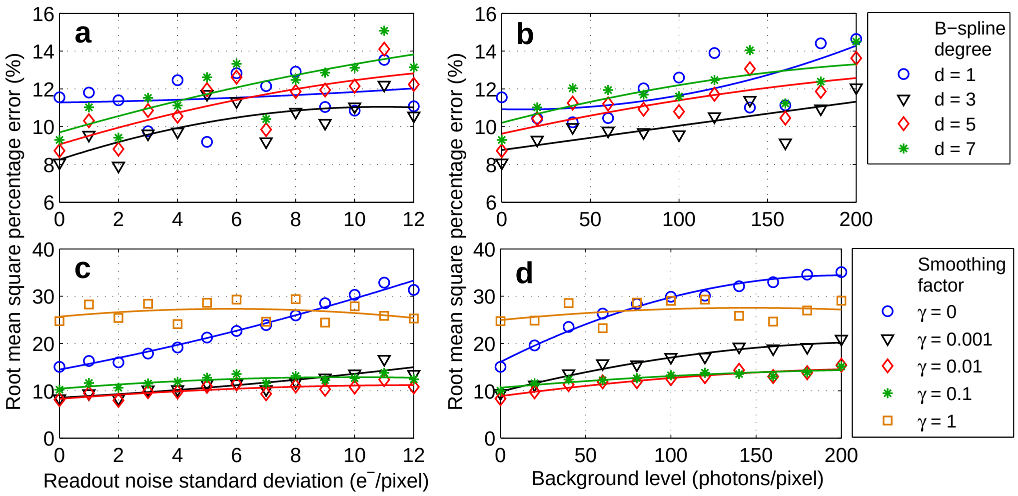

Figure 2.5: The effect of the B-spline degree and the smoothing factor on the error between analytical and experimental PLAMs in the presence of noise. (a), (b) The root mean square percentage error (see Eq. (2.17) for the definition) between the experimental and analytical PLAMs as functions of the standard deviation σ^c of the readout noise and background level b^c, respectively, for different B-spline degrees d. (c), (d) The same for different smoothing factors γ. In (a) and (b) the smoothing factor is set to 0.01 and in (c) and (d), the B-spline degree is set to 3. Each data point is the average of the errors for x_0-PLAM, y_0-PLAM and z_0-PLAM calculated over a z-range of [0.2, 0.9] μm. For the calculation of the PLAMs, we assumed a background level of $b = 10$ photons/pixel and a photon count of $N = 500$ photons. Other parameters are the same as those used in Fig. 2.4. Reprinted with permission from [34].

x_0-PLAM and the absolute deviation error over the z-range of [0, 0.8] μm. Although we assumed a significant amount of readout noise ($\sigma^c = 10$ e$^-$/pixel), the error is relatively small over the z-range of [0, 0.8] μm. Specifically, it is consistently smaller than 1.03 nm over this range (i.e. the average error is 3.2 %). Similar results are observed for the deduced experimental z_0-PLAM in the presence of noise (the average error over the z-range of [0, 0.8] μm is 11.7 %, see Fig. 2.4(f)).

However, the error between the experimental and analytical PLAMs is a function of the noise level, the B-spline degree and the smoothing factor. We next investigate this important dependence. For this purpose, we define the Root Mean Square Percentage

Error (RMSPE) as follows

$$\text{RMSPE} := 100 \times \left(\frac{1}{3P} \sum_{i=1}^{P} \left(\frac{x_0\text{-PLAM}_E(z_i) - x_0\text{-PLAM}_A(z_i)}{x_0\text{-PLAM}_A(z_i)} \right)^2 + \left(\frac{y_0\text{-PLAM}_E(z_i) - y_0\text{-PLAM}_A(z_i)}{y_0\text{-PLAM}_A(z_i)} \right)^2 + \left(\frac{z_0\text{-PLAM}_E(z_i) - z_0\text{-PLAM}_A(z_i)}{z_0\text{-PLAM}_A(z_i)} \right)^2 \right)^{1/2}, \tag{2.17}$$

where PLAM_E and PLAM_A denote the experimental and analytical PLAMs, respectively, and $z_i \in [0.2, 0.9]$ μm, for $i = 1, \ldots, P$. This integral error proves to be useful for studying the dependence of the experimental PLAM on the noise level, since it combines the errors in x_0-, y_0- and z_0-PLAMs in a single measure. This error is plotted in Figs. 2.5(a) and 2.5(b) as a function of the standard deviation of the readout noise and the background level, respectively, for different B-spline degrees. Not surprisingly, the error is on average monotonically increasing with the noise level regardless of the degree of the B-spline. At small noise levels, high B-spline degrees yield smaller errors than small B-spline degrees whereas this is reversed at high noise levels. For instance, the error levels for the B-splines of degree $d = 1$ and degree $d = 7$ are 11.2 % and 9.3 %, respectively, when the standard deviation of the readout noise is $\sigma^c = 0$ e^-/pixel (see Fig. 2.5(a)). On the other hand, at $\sigma^c = 12$ e^-/pixel, the aforementioned error levels change to 12 % and 13.82 %, respectively. Importantly, for noise levels that are typically observed in practice, i.e. readout noise with standard deviations 0 to 12 e^-/pixel and background levels 0 to 200 photons/pixel, a B-spline of degree 3 appears to provide the smallest amount of error. Specifically, for a cubic B-spline the error remains in the range of 8 % to 11 % for the mentioned noise levels (see Figs. 2.5(a) and 2.5(b)).

Figs. 2.5(c) and 2.5(d) show the error as a function of the standard deviation of the readout noise and the background level, respectively, for different smoothing factors. When the smoothing factor is zero, the error significantly increases with increasing noise level (e.g. it increases from 15 % to 35 % as the background level increases from 0 to 200 photons/pixel). As we increase the smoothing factor (e.g. to 0.001), the numerical values of the error decrease and the error becomes less dependent to the changes in the noise level. A relatively small smoothing factor of 0.01, for example, yields a relatively robust curve to the noise (with this smoothing factor, the error increases only from 8.9 % to 14.3 % as the background level increases from 0 to 200 photons/pixel). On the other hand, a large smoothing factor (e.g. $\gamma = 1$) leads to an over-smoothed spline fit. The loss of information due to over-smoothing, in turn, results in a large error (see Figs. 2.5(c) and 2.5(d)). Consequently, a relatively small smoothing factor (e.g. 0.005 to 0.05) can be an appropriate choice for typical noise levels in practice.

2.4.3 Experimental PSF example

In this section, we provide an example to investigate the performance of the proposed approach in practice. In particular, we collect the 3D experimental PSF of a microscopy setup using the procedure described in Section 2.2.1. We have deliberately used a setup with an aberrated PSF as it is a good example to illustrate the practical performance of the proposed approach. Figs. 2.6(a) and 2.6(b) show the yz- and xy-projections of the acquired experimental PSF, respectively. To suppress the stochasticity and noise in the collected experimental PSF, based on the analyses reported in the previous section, we fit a volume smoothing spline of appropriate degree and smoothing factor to the experimental PSF. The yz- and xy-projections of the smoothing spline fit are shown in Figs. 2.6(a’) and 2.6(b’), respectively, where we see a substantial suppression of the extraneous noise.

We further calculate the experimental x_0-PLAM and z_0-PLAM along the z-axis, which are shown in Figs. 2.6(c) and 2.6(d), respectively (the experimental y_0-PLAM is analogous to x_0-PLAM and is not shown). The experimental x_0-PLAM has smaller numerical values at or close to the plane of focus and increases as the particle moves away. This is an expected result for typical 3D PSFs (e.g. the Born and Wolf PSF) [26]. A subtle point in the behavior of the experimental x_0-PLAM is that it is not symmetric w.r.t. the plane of focus. For example, the numerical value of the x_0-PLAM is 30 nm at $z_0 = -0.6$ μm, whereas it is approximately 26 nm at $z_0 = 0.6$ μm. This is not surprising since any mismatch between the refractive indices of the sample and immersion medium contributes

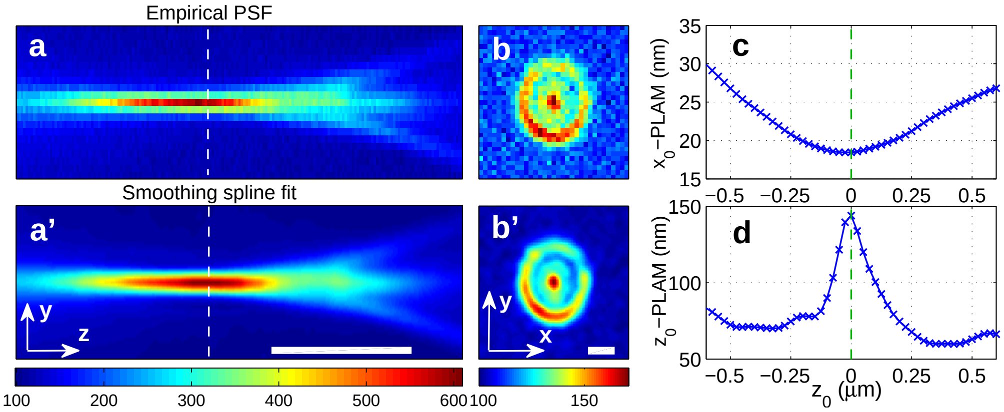

Figure 2.6: A practical example. (a), (b) The yz-projection and the xy-projection (at $z_0 = 2.6$ μm) of a deliberately aberrated experimentally collected PSF from a practical microscopy setup, respectively, where the ROI size is 33 × 33 pixels (for information regarding other parameters see Section 2.2.1). (a’), (b’) The corresponding yz- and xy-projections of the cubic volume spline fit with a smoothing factor of $\gamma = 0.01$, which is evaluated on a finer grid (color scale bars are in photons). The vertical dashed lines show the location of the plane of focus and the size bars are 1.5 μm (panels (a) and (a’) are stretched in the z-direction for better visualization while their scale in the y-direction is the same as panels (b) and (b’)). The estimated photon count and background level of the bead sample are approximately $N^c = 4500$ photons and $b^c = 16$ photons/pixel, respectively. (c), (d) The experimental x_0-PLAM and z_0-PLAM, respectively, along the z-axis (the reported results are the average of the results for multiple beads). For the calculation of the experimental PLAMs we assumed $N = 500$ photons and $b = 10$ photons/pixel. Reprinted with permission from [34].

to an axially asymmetric PSF [33].

Additionally, the experimental z_0-PLAM is large near or at the focal plane, e.g. it is 144 nm at the focal plane, and decreases as the point source moves away from the focal plane (see Fig. 2.6(d)). The large numerical value of the experimental z_0-PLAM at the focal plane is sometimes referred to as the depth discrimination problem and is expected (see e.g. [26]). The axial asymmetry of the z_0-PLAM can also be explained by the axial asymmetry of the PSF caused by the mismatch between the refractive indices of the sample and immersion oil [33].

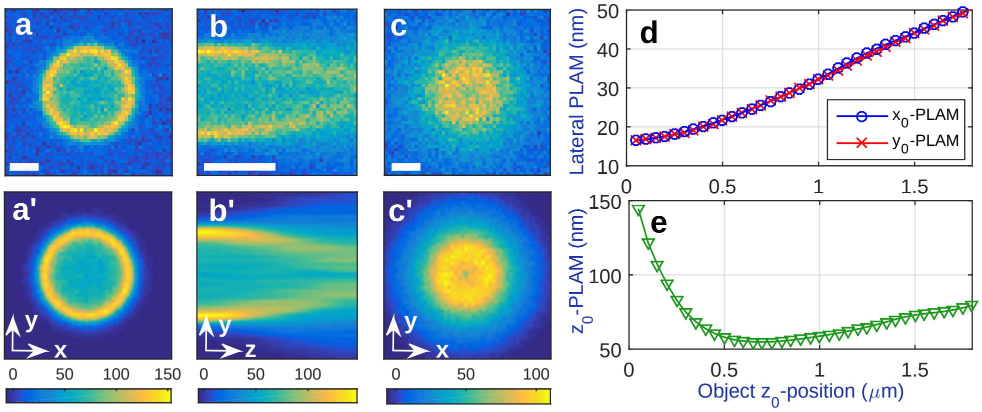

Figure 2.7: The experimental PLAM for a spherical shell. (a) The xy-projection at $z_0 = 0$ μm, (b) the yz-projection ($z_0 \in$ [-0.1, 2.2] μm) and (c) the xy-projection at $z_0 = 1.8$ μm of the simulated 3D image set of a spherical shell with internal and external radii of 1.5 μm and 1.8 μm, respectively, where the ROI size is 49 × 49 pixels. The image set was obtained by convolving the simulated object with the Born and Wolf 3D PSF model. We considered Poisson statistics, background and readout noise, where the standard deviation σ^c is 4 e$^-$/pixel, the background level b^c is 10 photons/pixel and the photon count N^c is 60000 photons. We assumed a 100x, NA 1.4 objective lens with $n_{\mathrm{oil}} = 1.515$. The pixel size, the z-step size and the emission wavelength are 13 μm × 13 μm, 50 nm and 690 nm, respectively. (a'), (b') and (c') The corresponding xy-, yz- and xy-projections of the cubic volume spline fit with a smoothing factor of $\gamma = 0.015$, which is evaluated on a finer grid (color scale bars are in photons). The focal plane is located at 0 μm and the size bars are 1 μm (panels (b) and (b') are stretched in the z-direction for better visualization while their scale in the y-direction is the same as panel (a)). (d), (e) The experimental x_0-PLAM (y_0-PLAM) and z_0-PLAM, respectively, along the z-axis. For the calculation of the experimental PLAMs, we assumed a background level of $b = 20$ photons/pixel and a photon count of $N = 5000$ photons. Reprinted with permission from [34].

2.4.4 Spherical shell example

As mentioned earlier, the proposed approach allows the calculation of the PLAM for general experimental objects. This section provides an example for the calculation of the experimental PLAM for such general objects. In particular, we simulated the 3D image set for a spherical shell by convolving the simulated 3D object with the 3D PSF of the optical system which was assumed to be the Born and Wolf model, and by considering the stochasticity due to Poisson statistics and extraneous noise sources (see Figs. 2.7(a)–2.7(c)). We then fit a volume smoothing spline to the experimental image set (see Figs. 2.7(a')–

2.7(c')). We supposed that at $z_0 = 0$ the equator of the spherical shell is in focus and calculated the experimental PLAM for this 3D object as it moves along the z-axis.

As shown in see Fig. 2.7(d), the experimental x_0- and y_0-PLAM are small when the object is in focus and increase as the object moves away from the plane of focus. This is an expected result and is analogous to the behavior of the x_0- and y_0-PLAM for a point source. Interestingly, the experimental z_0-PLAM is large when the object is at or near the plane of focus which implies that the z_0-position of the object cannot be estimated accurately (see Fig. 2.7(e)). This behavior is analogous to the depth discrimination problem for point sources [26]. For instance, the experimental z_0-PLAM is 108 nm when the object is 150 nm away from the plane of focus. This is mainly due to the fact that the image profiles of slices of a spherical shell near its equator appear similar (e.g. Fig. 2.7(a')). By increasing the z_0, the experimental z_0-PLAM reduces significantly. For example, at $z_0 = 700$ nm, the experimental z_0-PLAM is 54 nm. Further increasing the z_0, gradually worsens the experimental z_0-PLAM. The reason for this behavior is that at very large z_0-positions, the image profiles of the object become spread out over many pixels and, as such, the photon count per pixel will be negligible compared to the noise level.

2.4.5 Experimental non-point source example

Following the previous section, we now provide an experimental example for the calculation of the PLAM for non-point-like objects. Specifically, we imaged lysosomal compartments in live cells as described in Section 2.2.2 (see Fig. 2.8(a)). Figs. 2.8(b) and 2.8(c) show two individual lysosomal compartments. We fitted surface smoothing splines to these images (see Figs. 2.8(b') and 2.8(c')) and calculated the experimental PLAM. Using the proposed algorithm, the experimental PLAM can be calculated for any arbitrary photon count and noise level. Here we assumed a background level of 20 photons/pixel and a photon count of 5000 photons. The results are shown in Fig. 2.8(d). For instance, for the lysosome shown in Fig. 2.8(b) the experimental x_0- and y_0-PLAMs are 11.52 nm and 12.86 nm, respectively.

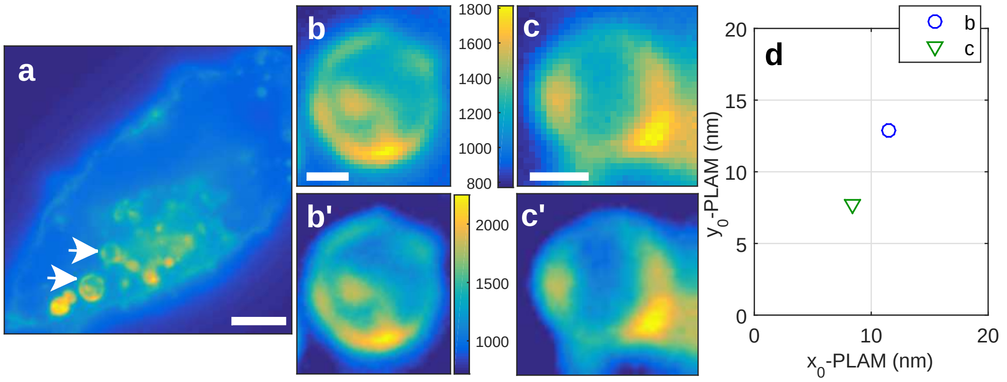

Figure 2.8: The experimental PLAM for lysosomes. (a) The image of a 22Rv1 cell transfected with mRFP-LAMP-1 which was acquired as described in Section 2.2.2. (b) and (c) The images of two individual lysosomal compartments marked by arrows in panel (a). All of the imaging parameters are reported in Section 2.2.2. (b') and (c') The corresponding cubic surface spline fit of the lysosomes with a smoothing factor of $\gamma = 0.01$, which is evaluated on a finer grid (color scale bars are in photons). The size bar in panel (a) is 3.8 μm and other size bars are 0.645 μm. (d) The experimental x_0-PLAM and y_0-PLAM for the lysosomes. For the calculation of the experimental PLAMs, we assumed a background level of $b = 20$ photons/pixel and a photon count of $N = 5000$ photons. Reprinted with permission from [34].

3. DESIGNING THE FOCAL PLANE SPACING FOR MULTIFOCAL PLANE MICROSCOPY*

3.1 Introduction

The development of MUM in the recent past has made it possible to track the 3D dynamics in live cells at high temporal and spatial resolution by simultaneously imaging different focal planes within the sample [36, 61, 63–67]. MUM overcomes the depth discrimination problem of conventional single plane microscopy and thereby allows high accuracy localization of subcellular structures and single molecules along the z-axis [44, 64, 68, 69]. MUM has been used to study different biological problems [26, 32, 70, 71]. For instance, in [70] MUM is used to understand the effect of tubulovesicular transport carriers on intracellular trafficking pathways within 3D cellular environments. Furthermore, in [32] MUM is utilized to study the 3D dynamics of single molecules in live epithelial cells.

One of the important questions in the design of MUM experiments concerns selecting the appropriate spacings between the focal planes. Varying the plane spacing changes the image profiles of the object of interest (e.g. a point source) at the focal planes. An implication of changes in the image profiles is that the accuracy for localizing the object as it moves along the z-axis will be affected [26]. Another implication is that the object of interest may become difficult to detect in the acquired image. For instance, the image profile at a focal plane far from the object of interest will be diffusely spread out, making the object both difficult to localize and difficult to detect with respect to that focal plane. As a consequence, for a given MUM setup the choice of the plane spacing determines whether a point source can be localized with a consistent level of accuracy, and whether it can be continuously detected by the imaging system, as it moves along the z-axis.

In addition to the plane spacing, selecting the appropriate number of focal planes to

---

*Reprinted with minor modifications, with permission from "Designing the focal plane spacing for multifocal plane microscopy" by A. Tahmasbi, S. Ram, J. Chao, A. V. Abraham, F. W. Tang, E. S. Ward, and R. J. Ober, 2014. Opt. Express, vol. 22, no. 14, pp. 16706-16721, Copyright 2014 by Optical Society of America.

cover a sample of a certain thickness is also of importance in the design of MUM experiments. Different authors have used different numbers of planes to cover their desired viewing and tracking depth, i.e. a range along the z-axis over which the particle is detectable by the imaging system. For instance, in [71] a 4-plane MUM setup, covering a 2 μm depth, is utilized to study the dynamics of tubulovesicular transport containers. In [32] a 4-plane MUM setup providing a 10 μm viewing and tracking depth is used to study the 3D single molecule dynamics in live epithelial cells. More recently, in [72] a 9-plane MUM setup is developed that provides a viewing and tracking depth of $2.25 - 18$ μm. Increasing the number of focal planes can enhance the viewing and tracking depth. However, in fluorescence microscopy experiments, regardless of the number of focal planes, a specific number of photons is collected from the sample per acquisition. This fixed number of photons is then split among multiple focal planes. Hence, each plane detects fewer photons when the number of planes is increased. A poorer localization accuracy might therefore be obtained when using a large number of planes. This is due to the fact that decreasing the number of detected photons at each focal plane worsens the localization accuracy of the MUM setup [13, 26].

In this paper, we address the above concerns by investigating the PLAM for a MUM setup. The PLAM provides the best possible accuracy (standard deviation) with which an isolated single molecule can be localized, and it is calculated using the Fisher Information Matrix [13, 41, 73]. The latter represents the amount of information the data provides about an unknown parameter [42]. For our analysis, we consider two design requirements that are typically encountered while setting up MUM experiments. The first requirement is to achieve a relatively constant PLAM along the z-axis such that the 3D location of a subcellular structure or single molecule can be estimated with the same level of accuracy across the viewing and tracking depth. The second requirement is to allow for a relatively large viewing and tracking depth across the sample in order to cover the z-range over which the cellular process of interest occurs. Taking into account these design considerations, we provide guidelines to set up appropriate MUM experiments for different applications. Aside from the number of planes and their spacings, a variety of other imaging parameters such as photon count, system magnification and the numerical aperture of the objective lens also influence the PLAM. Here, we also examine the effect of these parameters on the plane spacing.

In practice, the calculation of the PLAM is computationally expensive. Thus, without appropriate software determining the appropriate number of focal planes and their spacing can be a complicated and time consuming procedure. We therefore also introduce a new software module called MUMDesignTool that calculates and plots the PLAM along the z-axis and provides a user-friendly framework for finding the appropriate number of planes and plane spacings for a MUM setup. The results of the paper can be reproduced using the MUMDesignTool.

3.2 Simulations

The results of this paper are calculated using a new software module, the MUMDesignTool, developed in the MATLAB environment (The MathWorks Inc., Natick, MA). The software is available at *http://www.wardoberlab.com/* and its detailed description can be found in Section 3.4.8. Using this software we model an isolated single molecule that is imaged by a pixelated detector in the presence of background and readout noise [13]. A Poisson process models the background effect and a Gaussian process models the readout noise of the detector. The pixel dimensions are 13 μm × 13 μm. We assume the PSF is given by the Born and Wolf model [10]. The emission wavelength is assumed to be the same for all focal planes. The refractive index n_{oil} of the immersion oil is 1.515. The tube length L of the microscope is 160 mm. The remaining parameters are given below each figure.

3.3 Theory

3.3.1 Behavior of the PLAM and the Fisher information matrix for a MUM setup

In this section, we briefly review the concepts concerning the PLAM and define several terms which are necessary for our later discussions. For all of our analysis we assume that a single molecule is modeled as a point source. We denote the best possible localization accuracy that can be achieved for estimating the x, y and z coordinates of the single molecule by x_0-PLAM, y_0-PLAM and z_0-PLAM (axial-PLAM), respectively. The PLAMs are calculated using the well-known CRLB [42,74], which is specified in terms of the inverse of the FIM. The FIM represents the amount of information the data provides about an unknown parameter of interest which in the current case pertains to the 3D location of the single molecule [42, 43]. We refer to the amount of information about the x, y and z coordinates of the single molecule as x_0-FIM, y_0-FIM and z_0-FIM (axial-FIM). Large numerical values of x_0-FIM, y_0-FIM and axial-FIM, which correspond to small values of x_0-PLAM, y_0-PLAM and axial-PLAM, respectively, specify a better localization accuracy.

The FIM and therefore the PLAM depend on a variety of imaging parameters such as the numerical aperture of the objective lens, the magnification, the emission wavelength, the photon count and the z-position of the point source. The behavior of the PLAM as a function of the mentioned parameters can be explained through the mathematical expression of the FIM. This paper is primarily devoted to the investigation of the effect of these parameters on the PLAM, in the context of MUM, with an emphasis on the effect of the z-position of the point source with respect to the focal planes.

Here, we express the FIM for a MUM setup for a general single molecule microscopy experiment. Let $\Theta \subseteq \mathbb{R}^3$ be an open parameter space and let $\theta = (x_0, y_0, z_0) \in \Theta$ be the vector of unknown parameters representing the 3D location of a single molecule in the object space with respect to the design focal plane, i.e. the standard infinity-corrected focal plane in conventional single plane microscopy. Consider a pixelated detector $\left\{C_1, \ldots, C_{K_{pix}}\right\}$ which consists of K_{pix} pixels, where $C_k \subseteq \mathbb{R}^2,\ k = 1, \ldots, K_{pix}$, denotes the area occupied by the k^{th} pixel. Assume that the pixels are disjoint. Suppose that we have K_{pln} focal planes where the first plane is equivalent to the design focal plane. It has been shown that the photon counts detected by the pixels of the n^{th} plane due to a single molecule axially located at z_0 are realizations of independent Poisson random variables with expected values [13,43]

$$\mu_{\theta,n}(k) := N_n\tilde{\mu}_{\theta,n}(k) = \frac{N_n}{M_n^2}\int_{C_{k,n}} q_{z_0-\Delta z_{1n}}\left(\frac{x}{M_n}-x_0, \frac{y}{M_n}-y_0\right)dxdy,$$
$$\theta \in \Theta \subseteq \mathbb{R}^3,\ n=1,\ldots,K_{pln},\ k=1,\ldots,K_{pix},$$

where N_n is the expected number of detected photons on the n^{th} infinite detector plane (i.e. $\mathbb{R}^2$) due to the single molecule such that $\sum_{n=1}^{K_{pln}} N_n = N_{tot}$, with N_{tot} denoting the total number of detected photons due to the single molecule on an arbitrarily positioned infinite detector plane (i.e. $\mathbb{R}^2$). Note that N_{tot} is independent of the number of focal planes. The term $C_{k,n}$ denotes the k^{th} pixel at the n^{th} focal plane. In addition, M_n is the lateral magnification at the n^{th} focal plane, Δz_{1n} is the distance between the design focal plane and the n^{th} focal plane in the object space (with $\Delta z_{11} = 0$) and q_{z_0} is the image function [13,26].

The image function describes the image of a stationary single molecule on the detector at unit lateral magnification when the single molecule is located on the z-axis in the object space. Here, we assume that the image function is given by the Born and Wolf 3D PSF (for more information see [10,26]). Moreover, it has been previously shown, under geometrical optics, that the lateral magnification for a focal plane that is shifted by a distance of Δz_{1n} from the design focal plane is given by [75]

$$M_n := M(\Delta z_{1n}) = M_1\frac{L - \frac{LM_1^2\Delta z_{1n}}{n_{oil}L+M_1^2\Delta z_{1n}}}{L}, \qquad n=1,\ldots,K_{pln},\ \Delta z_{1n}\in\mathbb{R},$$

where n_{oil} is the refractive index of the immersion oil and L is the tube length of the microscope.

For a practical microscopy setup where the acquired data is corrupted by extraneous noise sources, the expression of the FIM for the parameter-vector θ at the n^{th} focal plane is given by [13,43,60]

$$\boldsymbol{I}_n(\theta) = \sum_{k=1}^{K_{pix}} \frac{\psi_n(k)}{\nu_{\theta,n}(k)} \left(\frac{\partial \mu_{\theta,n}(k)}{\partial \theta}\right)^T \frac{\partial \mu_{\theta,n}(k)}{\partial \theta}, \qquad \theta \in \Theta,\ n = 1, \ldots, K_{pln}, \tag{3.1}$$

where $\nu_{\theta,n}(k) = \mu_{\theta,n}(k) + b_{k,n}$ with $b_{k,n},\ k = 1, \ldots, K_{pix},\ n = 1, \ldots, K_{pln}$, denoting the photon count due to the background noise at pixel C_k and plane n. The term $\psi_n(k)$ is the so-called noise coefficient that depends on the type of detector [60]. In the absence of readout noise, $\psi_n(k) = 1$ for all $k = 1, \ldots, K_{pix},\ n = 1, \ldots, K_{pln}$ [13]. In the presence of readout noise and when using CCD and CMOS detectors, the noise coefficient is given by [13]

$$\psi_n(k) = \nu_{\theta,n}(k) \times \left(\frac{e^{-\nu_{\theta,n}(k)}}{\sqrt{2\pi}\sigma_{k,n}} \int_{\mathbb{R}} \frac{\left(\sum_{l=1}^{\infty} \frac{\nu_{\theta,n}^{l-1}(k)}{(l-1)!} e^{\frac{-(z-l-\eta_{k,n})^2}{2\sigma_{k,n}^2}} \right)^2}{\sum_{l=0}^{\infty} \frac{\nu_{\theta,n}^{l}(k)}{l!} e^{\frac{-(z-l-\eta_{k,n})^2}{2\sigma_{k,n}^2}}} dz - 1 \right),$$

where $\eta_{k,n}$ and $\sigma_{k,n}^2$ denote the mean and the variance of the readout noise, respectively, for $k = 1, \ldots, K_{pix}$ and $n = 1, \ldots, K_{pln}$. The expression of the noise coefficient in the presence of stochastic signal amplification and readout noise, i.e. when using an EMCCD detector, is omitted for brevity but can be found in [60].

Since the data acquisition in each focal plane is independent of the data acquisition in the other planes, the FIM of a MUM setup is the sum of the FIMs of the individual planes [26] and we have

$$\boldsymbol{I}_{MUM}(\theta) = \boldsymbol{I}_1(\theta) + \boldsymbol{I}_2(\theta) + \cdots + \boldsymbol{I}_{K_{pln}}(\theta), \qquad \theta = (x_0, y_0, z_0) \in \Theta. \tag{3.2}$$

For the current 3D localization problem, the FIM $\boldsymbol{I}(\theta)$ for any given focal plane or for the MUM setup is a 3 × 3 matrix. The main diagonal elements of this 3 × 3 matrix provide information about the x, y and z coordinates of the single molecule and we refer to them as the x_0-FIM, y_0-FIM and z_0-FIM (axial-FIM), respectively. According to the Cramér-Rao inequality [74], the covariance matrix of any unbiased estimator $\hat{\theta}$ of an unknown parameter θ is always greater than or equal to the inverse FIM, i.e. $\mathrm{cov}(\hat{\theta}) \geq \boldsymbol{I}^{-1}(\theta)$ [13,42]. Therefore, the square roots of the main diagonal elements of the inverse FIM provide lower bounds for the accuracy (standard deviation) with which the x, y and z coordinates of the single molecule can be estimated. We denote these lower bounds by x_0-PLAM, y_0-PLAM and z_0-PLAM (axial-PLAM), respectively. It is important to note that the PLAM has been previously validated by comparing it with the standard deviation of the estimated locations of single molecules in actual microscopy experiments (see e.g. [26]).

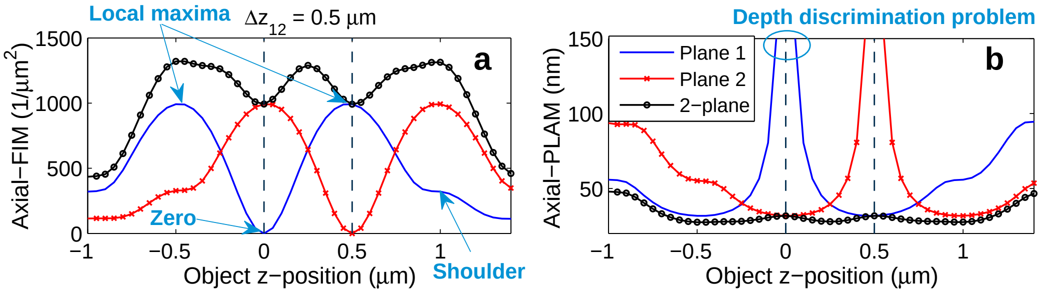

Figure 3.1: The behavior of the axial-FIM and the axial-PLAM for conventional microscopy and MUM. (a) The axial-FIM and (b) the axial-PLAM for a 2-plane MUM setup and two conventional single plane setups (Plane 1 and Plane 2) as a function of the z-position of the point source. The zero, local maxima and shoulders of the axial-FIM of Plane 1, and the depth discrimination problem can be seen in panels (a) and (b), respectively. The results are calculated for a 100x, NA 1.3 objective lens. The plane spacing (Δz_{12}) is 0.5 μm, the photon count is 250 photons/plane and the emission wavelength is 520 nm. The background level is 1 photon/pixel/plane and the standard deviation of the readout noise is 2 e^-/pixel. The ROI size is 11 × 11 pixels. Reprinted with permission from [31].

Fig. 3.1(a) shows the axial-FIM for a conventional single plane microscopy setup with a standard infinity-corrected (i.e. design) focal plane as a function of the z-position of the point source ("Plane 1"). For ease of reference, we denote this and its corresponding axial-PLAM by axial-FIM$_1$ and axial-PLAM$_1$, respectively. As can be seen, the axial-FIM$_1$ is zero when the object is at the focal plane, implying that the data does not provide any information about the z-location of the point source; we refer to this spot as the zero of the axial-FIM$_1$. A consequence of the zero of the axial-FIM$_1$ is the depth discrimination problem, implying that there is a high uncertainty in estimating the z-position of the point source when it is located near the focal plane [64, 73]. This problem is illustrated in Fig. 3.1(b) ("Plane 1"), which shows the axial-PLAM$_1$ increases without bound as the point source approaches Plane 1.

By moving the point source away from the focal plane the axial-FIM$_1$ increases and at some z-position the axial-FIM$_1$ reaches a peak which we refer to as the local maximum of the axial-FIM$_1$. Further moving the point source away from the focal plane gradually decreases the axial-FIM$_1$ and at some z-position the axial-FIM$_1$ has a bump which we refer to as the shoulder of the axial-FIM$_1$. The described behavior of the axial-FIM$_1$ is symmetric with respect to the z-position of the focal plane due to the axial symmetry of the Born and Wolf 3D PSF, which has been used to calculate the FIM [10].

Fig. 3.1(b) also shows the axial-PLAM for a 2-plane MUM setup along the z-axis. For brevity, we refer to this and its corresponding axial-FIM as axial-PLAM$_{MUM}$ and axial-FIM$_{MUM}$, respectively. As can be seen, the axial-PLAM$_{MUM}$ is relatively constant along the z-axis including at the focal planes when compared to the axial-PLAM for a conventional (single-plane) microscope (i.e. "Plane 1"). This implies that MUM overcomes the depth discrimination problem of conventional microscopy and allows high accuracy z-localization. This is due to the fact that the axial-FIM$_{MUM}$ is the sum of the axial-FIMs of the individual planes (i.e. axial-FIM$_1$ and axial-FIM$_2$) because of the independence of data acquisition at each focal plane (see Fig. 3.1(a)) [26, 64]. Hence, the axial-FIM$_{MUM}$ is nonzero for a range of z-positions including at the focal planes.

3.3.2 Graphical interpretation of the design of plane spacing for a MUM setup

We now give a graphical interpretation for the design of the focal plane spacing for a MUM setup. Our design objective is to obtain an appropriate level of the axial-PLAM for the MUM system. Due to the fact that the PLAM$_{MUM}$ is specified in terms of the inverse of the FIM$_{MUM}$, minimizing the axial-PLAM$_{MUM}$ is closely related to maximizing the axial-FIM$_{MUM}$. We carry out the main steps of the focal plane spacing design by investigating the axial-FIM as this will prove to be a very convenient criterion due to two important properties of the axial-FIM. First, as pointed out earlier, the axial-FIM$_{MUM}$ is the sum of the axial-FIMs for the planes that make up the MUM system (see also Appendix C). It is this additive property of the axial-FIMs that makes it very convenient to define the focal plane spacing problem in terms of the axial-FIMs rather than directly through the axial-PLAMs. Hence, as shown in Fig. 3.1(a), the axial-FIM$_{MUM}$ curve along the z-axis is obtained by adding the axial-FIM curves of the individual focal planes (i.e. axial-FIM$_1$ and axial-FIM$_2$ for the 2-plane configuration of Fig. 3.1). The second property of the axial-FIM which we need is that, to a good approximation, the graphs of axial-FIMs of the different focal planes are simply translated versions of the graph of the axial-FIM for the design focal plane along the z-axis (see Fig. 3.1(a)). We should note that this property is based on the assumption that different focal planes have similar experimental conditions, e.g. the photon count and extraneous noise, as would be the case if identical detectors are used and the emission light is equally split amongst the detectors for the different planes. This second property in particular implies that changing the position of a focal plane with respect to the other planes amounts to a corresponding translation of the graph of the axial-FIM.

These two properties immediately provide the basis for a graphical interpretation of the design process for focal plane spacing. The design process can therefore be thought of as shifting the graphs of the axial-FIMs such that their sum, i.e. the axial-FIM of the MUM configuration, has the desired values for the range of z-positions for the point source that are of interest. Building on the idea of shifting and adding the similar FIMs for the different focal planes, in Appendix C we develop a fast approach for the calculation of the FIM$_{MUM}$ that also accounts for focal planes with different photon counts.

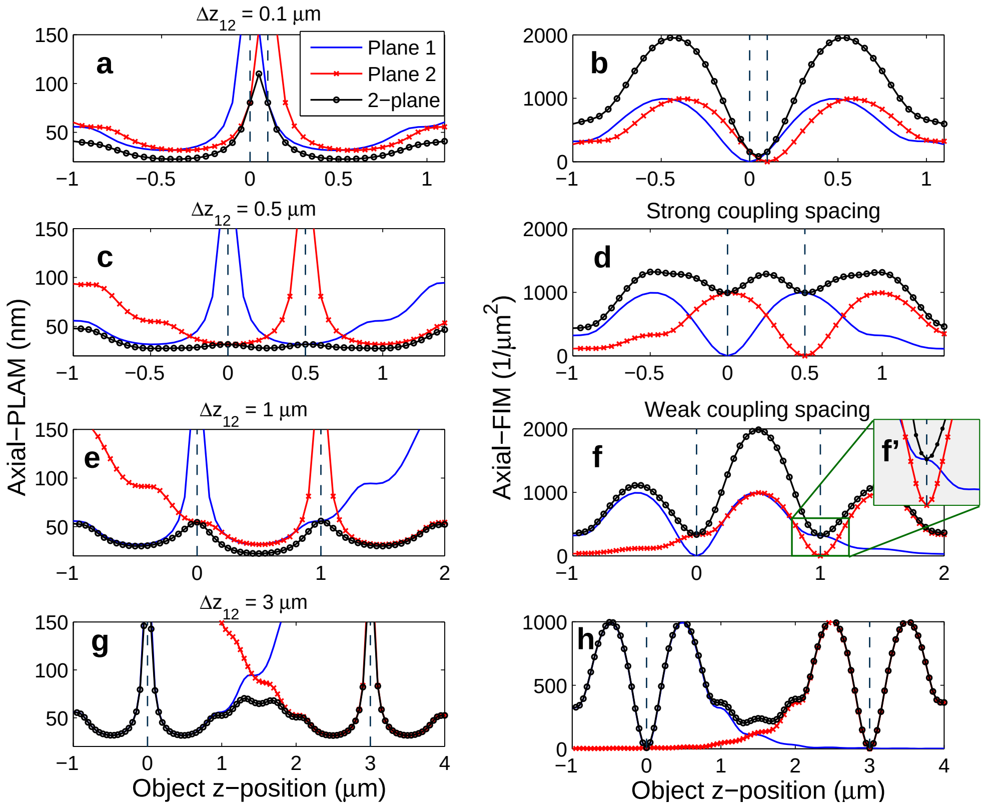

Figure 3.2: The effect of plane spacing on the axial-PLAM and the axial-FIM for a MUM setup. The left-hand (right-hand) side plots show the axial-PLAM (axial-FIM) for a 2-plane MUM setup as a function of the z-position of the point source. The figure also shows the axial-FIMs and axial-PLAMs of focal planes 1 and 2. The plane spacings (Δz_{12}) are 0.1, 0.5, 1 and 3 μm from top to bottom. (c) and (d) show the strong coupling spacing whereas (e) and (f) show the weak coupling spacing. (f’) shows the shoulder of the axial-FIM$_1$ more clearly. The results are calculated for a 100x, NA 1.3 oil immersion objective lens where the photon count is 250 photons/plane and the emission wavelength is 520 nm. The background level is 1 photon/pixel/plane and the standard deviation of the readout noise is 2 e$^-$/pixel. The ROI size is 11 × 11 pixels. Reprinted with permission from [31].

3.4 Results

3.4.1 *Strong and weak coupling spacings: constant z-localization accuracy*

An important requirement in the design of MUM experiments is to achieve a constant axial-PLAM$_{MUM}$ along the z-axis as it allows estimating the axial location of an object with a constant level of accuracy across the viewing and tracking depth. Here, as a first step we investigate the influence of different plane spacings on the axial-PLAM$_{MUM}$ assuming that the number of focal planes is two. In the subsequent sections, we will study MUM setups with more than two focal planes. The behavior of the axial-PLAM of a 2-plane MUM setup for different plane spacings is illustrated in the left-hand side plots of Fig. 3.2, where it is shown that altering the plane spacing changes the flatness of the curve. When the plane spacing is small ($\Delta z_{12} = 0.1$ μm), there is a significant variation in the axial-PLAM$_{MUM}$ value between the focal planes, i.e. the axial-PLAM$_{MUM}$ varies from 22 nm to 110 nm over the z-range of [-0.6, 1.1] μm (see Fig. 3.2(a)).

By increasing the plane spacing, the axial-PLAM$_{MUM}$ becomes more constant along the z-axis and a certain spacing ($\Delta z_{12} = 0.5$ μm) yields a relatively flat curve (see Fig. 3.2(c)). For this spacing, the axial-PLAM$_{MUM}$ varies from 28 nm to 31 nm over the same z-range of [-0.6, 1.1] μm. This relatively constant axial-PLAM$_{MUM}$ is achieved when the local maximum of the axial-FIM of the second plane (axial-FIM$_2$) falls on the zero of the axial-FIM of the first plane (axial-FIM$_1$), as shown in Fig. 3.2(d). We refer to this spacing as the strong coupling spacing. Further increasing the plane spacing worsens the flatness of the curve (see Fig. 3.2(e)). Hence, we set the largest acceptable plane spacing to be the case where the shoulder of the axial-FIM$_2$ overlaps with the zero of the axial-FIM$_1$, which can be seen in Figs. 3.2(f) and 3.2(f'). We refer to this spacing as the weak coupling spacing. For this spacing, the axial-PLAM$_{MUM}$ varies from 23 nm to 54 nm over the z-range of [-0.6, 1.1] μm, as can be seen in Fig. 3.2(e) (note that the variation also remains unchanged over the larger z-range of [-1, 2] μm).

A very large plane spacing ($\Delta z_{12} = 3$ μm) results in significant variations in the curve, with large axial-PLAM$_{MUM}$ values both between the focal planes and at the focal planes, i.e. the axial-PLAM$_{MUM}$ varies from 31 nm to 381 nm over the z-range of [-0.6, 1.1] μm (see Fig. 3.2(g)). The latter is due to the fact that the axial-FIMs of two distantly spaced focal planes make small contributions to the axial-FIM$_{MUM}$ at the focal planes (see Fig. 3.2(h)). Hence, the axial-PLAM$_{MUM}$ at each focal plane is large. In other words, two distantly spaced focal planes are similar to two separate conventional microscopy setups.

3.4.2 Lateral-PLAM and constant x- and y-localization accuracy along the z-axis

Aside from a constant z-localization accuracy, achieving constant x- and y-localization accuracy is also of importance in the context of 3D tracking. Here, we analyze the behavior of the x_0-PLAM and y_0-PLAM for a MUM setup along the z-axis. For this purpose, we define the lateral-PLAM as the square root of the sum of $(x_0\text{-PLAM}_{MUM})^2$ and $(y_0\text{-PLAM}_{MUM})^2$. The lateral-PLAM quantifies the best possible accuracy for the lateral localization of a particle. A large value for the lateral-PLAM at a certain z-position implies a poor lateral localization accuracy at that z-position.

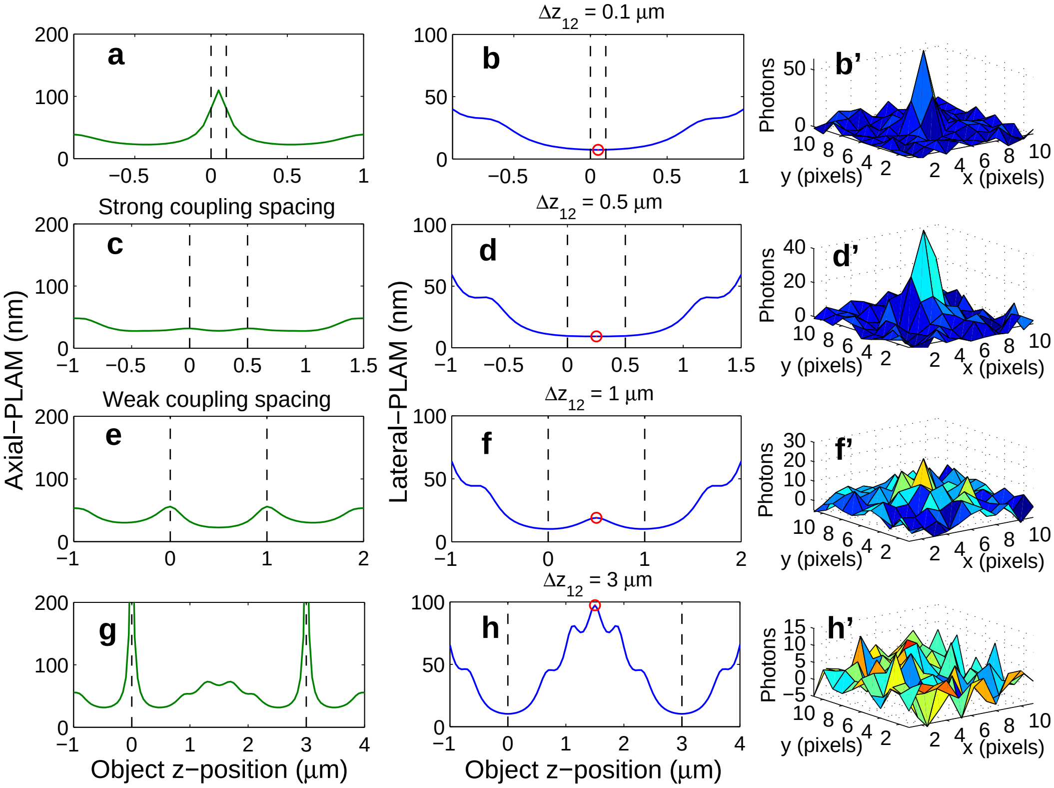

Figure 3.3: The behavior of the lateral-PLAM. The left and middle columns show the axial-PLAM and the lateral-PLAM, respectively, for a 2-plane MUM setup as a function of the z-position of the point source. The plane spacings (Δz_{12}) are 0.1, 0.5, 1 and 3 μm from top to bottom. The right column shows the mesh plots of the simulated images of point sources located at z-positions shown by the red circles on the design plane. The simulation parameters are identical to those used in Fig. 3.2. Reprinted with permission from [31].

Fig. 3.3 shows the axial-PLAM and the corresponding lateral-PLAM for a 2-plane MUM setup for different plane spacings. All imaging conditions are the same as those used for Fig. 3.2. When the focal planes are located close to one another ($\Delta z_{12} = 0.1$ μm), the lateral-PLAM varies from 7.3 nm to 32.6 nm over the z-range of [-0.3, 0.8] μm (see Fig. 3.3(b)). Adjusting the plane spacing based on the strong coupling spacing (Fig. 3.3(c)) and the weak coupling spacing (Fig. 3.3(e)) provides relatively constant lateral-PLAMs. More specifically, for the strong coupling spacing the lateral-PLAM varies from 9.2 nm to 13.7 nm over the z-range of [-0.3, 0.8] μm (Fig. 3.3(d)), whereas for the weak coupling spacing it varies from 10.1 nm to 19 nm over the same z-range (Fig. 3.3(f)). For a large plane spacing ($\Delta z_{12} = 3$ μm), the lateral-PLAM varies significantly, i.e. from 10.3 nm to 45.1 nm, over the same z-range (see Fig. 3.3(h)) which implies that the lateral location of the particle cannot be estimated with a constant level of accuracy.

3.4.3 Large viewing depth for qualitative imaging applications

In the previous sections, we analyzed the effect of plane spacing on the 3D localization accuracy of a point source along the z-axis and discussed spacing scenarios for quantitative 3D tracking using MUM. In some imaging applications, however, the objective is the qualitative 3D visualization of events. An example of such applications is the trafficking of receptors from sorting endosomes to the plasma membrane [71]. A key requirement in such cases is that the particle/structure is continuously detectable in the acquired data as it moves within the sample. Here, by making use of the lateral-PLAM, we investigate how the plane spacing affects the visual identifiability of a particle in a MUM setup.

By definition, a large value of the lateral-PLAM predicts poor lateral localization accuracy, which can also be interpreted as high uncertainty in visually detecting the particle in the acquired image. Fig. 3.3 (middle panels) shows the behavior of the lateral-PLAM for different plane spacings for a 2-plane MUM setup. For a small plane spacing ($\Delta z_{12} = 0.1$ μm), the numerical value of the lateral-PLAM at the midpoint between the focal planes is relatively small, i.e. 7.3 nm. Correspondingly, the point source can be clearly visually identified in a MUM image as shown in the mesh plot (Fig. 3.3(b'), where only the image from the first focal plane is shown). As the plane spacing increases, the numerical value of the lateral-PLAM varies significantly such that at a certain plane spacing the point source becomes barely detectable in the image. For example, for a plane spacing of 1 μm that corresponds to the weak coupling spacing, the lateral-PLAM for a point source at $z = 0.5$ μm is 19 nm and at this position the particle is marginally visible in the image (see Fig. 3.3(f')). For larger plane spacings the particle can no longer be identified in the image (Fig. 3.3(h')). This is due to the fact that as the plane spacing increases, for certain z-positions (especially near the midpoint between the focal planes), the distance between the particle and each focal plane becomes so large that the particle is significantly out of focus and is therefore undetectable in the image.

Thus, from the above discussion we see that the weak coupling scenario provides a guideline for adjusting the plane spacing to achieve a large viewing range and helps in designing MUM setups, for example, to observe a particular cellular process that occurs over a large z-range.

3.4.4 Effects of numerical aperture, magnification and emission wavelength on the spacing scenarios

The FIM of a MUM setup depends on a second group of parameters such as the numerical aperture, magnification and emission wavelength. Therefore, in this section we investigate how these factors affect the plane spacings. We first study the effect of numerical aperture. Fig. 3.4(a) shows the effect of changing the numerical aperture on the strong and weak coupling spacings, where we observe an inverse dependence of the spacings on the numerical aperture assuming that all other parameters remain the same. For instance, the strong coupling spacing increases from $\Delta z_{sc} = 0.35$ μm to $\Delta z_{sc} = 0.75$ μm (i.e. a 114% elongation) when the numerical aperture decreases from 1.4 to 0.95. This implies that a low NA objective supports relatively constant 3D localization accuracy over a larger viewing and tracking depth than a high NA objective. This result is not surprising considering the fact that given a low NA objective, the PSF has a broader profile in the xz-plane and/or the yz-plane. The broader profile leads to a stretched axial-FIM along the z-axis

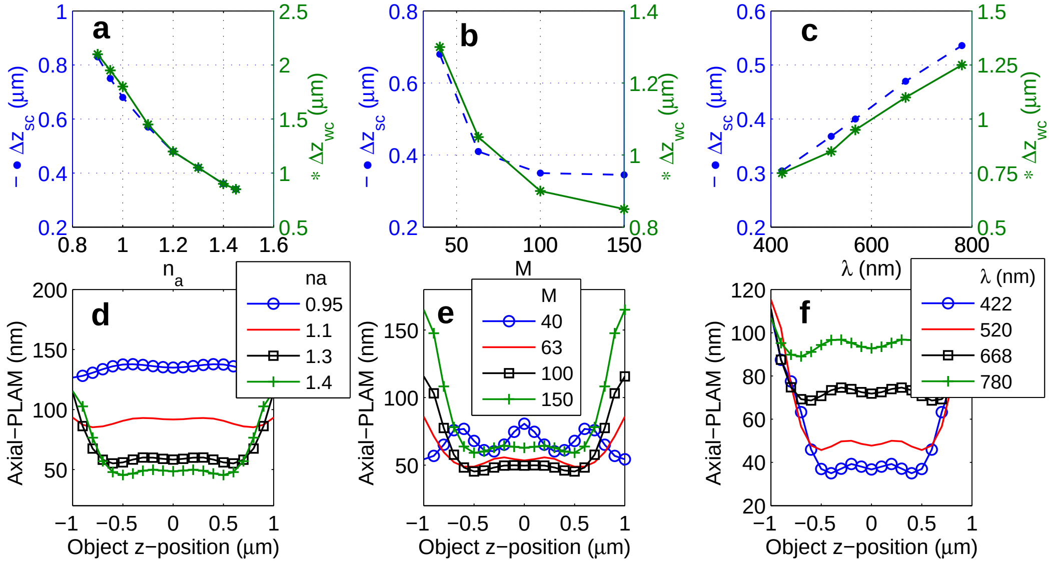

Figure 3.4: The effect of changing imaging parameters on the spacing scenarios. A plot of the strong coupling spacing (Δz_{sc}) and weak coupling spacing (Δz_{wc}) versus (a) the numerical aperture n_a, (b) magnification M and (c) emission wavelength λ. (d), (e) and (f) show the axial-PLAM for a 2-plane MUM setup as a function of the z-position of the point source for different numerical apertures, magnifications and emission wavelengths, respectively. In (d), (e) and (f), the plane spacings are adjusted based on the strong coupling scenario. The photon count is 250 photons/plane. The ROI size is 32 × 32 pixels. The magnification is 100, the emission wavelength is 520 nm and the numerical aperture is 1.4. The background level and the standard deviation of the readout noise are 2.5 photons/pixel/plane and 8 e^-/pixel, respectively. Reprinted with permission from [31].

for each focal plane and thereby it is expected that a low NA objective leads to a more constant axial-PLAM$_{MUM}$ along the z-axis. However, the numerical value of the axial-PLAM$_{MUM}$ for the low NA objective along the z-axis is typically higher than that of a high NA objective (Fig. 3.4(d)). For example, for a 1.1 NA objective, the axial-PLAM$_{MUM}$ varies from 85 nm to 93 nm over the z-range of [-0.8, 0.8] μm. Over the same z-range, the numerical value of the axial-PLAM$_{MUM}$ for a 1.4 NA objective varies from 45 nm to 77 nm. This is also an expected result given the fact that use of a low NA objective yields a broader image profile in the xy-plane, which translates to a poorer localization accuracy. We note that an analogous behavior is also observed for the weak coupling spacing (not shown). The high numerical value of the axial-PLAM$_{MUM}$ for the 0.95 NA objective can be reduced in part by collecting more photons from the sample due to the inverse dependence of the PLAM on the photon count. Thus, an immediate implication of this result is that depending on the requirements for the viewing and tracking depth and the desired level of 3D localization accuracy, it is necessary to make a careful choice of experimental parameters (e.g. numerical aperture of the objective lens) and imaging conditions (photon count/signal from the sample).

We next examine the effect of magnification on the spacing scenarios. Analogous to the behavior with respect to the numerical aperture, the strong and weak coupling spacings increase with decreasing values of magnification assuming all other parameters are the same (Fig. 3.4(b)). More specifically, as the magnification decreases from 150x to 40x the strong coupling spacing increases from 0.35 μm to 0.68 μm. However, as shown in Fig. 3.4(e), the behavior of the axial-PLAM$_{MUM}$ as a function of z-position for different magnification values exhibit a distinct behavior. As the magnification increases from 40x to 63x, the numerical value of the axial-PLAM$_{MUM}$ for a z-range of [-0.8, 0.8] μm varies from 60 nm to 81 nm, and from 49 nm to 59 nm, respectively. This implies that with increasing magnification values, one can expect relatively constant z-localization accuracy over a certain z-range. However, this behavior is true only up to a certain point. For instance, for a magnification of 150x the axial-PLAM$_{MUM}$ value exhibits greater variation, i.e. from 59 nm to 108 nm over the z-range of [-0.8, 0.8] μm when compared to a 100x magnification for which the axial-PLAM$_{MUM}$ varies from 46 nm to 77 nm over the same z-range. This is due to the fact that at very high magnifications, the image of the point source is spread out over such a large number of pixels that the number of photons detected from the point source at each pixel becomes relatively small compared to the readout noise. This results in the observed variation in the axial-PLAM$_{MUM}$, which depends not only on the total number of detected photons but also on the spatial distribution of the detected photons over the pixels [26, 71].

We last study the behavior of the spacing scenarios as a function of the emission wavelength. Increasing the emission wavelength increases the strong and weak coupling spacings (see Fig. 3.4(c)). As a consequence, a fluorophore with a large emission wavelength can provide a relatively constant level of accuracy across a larger viewing and tracking depth (see Fig. 3.4(f)). Similar to the discussion regarding the numerical aperture, the PSF given a large emission wavelength has a broader profile in the xz-plane (or yz-plane) and thereby one would expect a large emission wavelength to yield a more constant axial-PLAM$_{MUM}$ along the z-axis.

3.4.5 Effects of photon count and extraneous noise on the spacing scenarios

We next investigate the dependence of the strong and weak coupling spacings on the photon count and readout noise. In the presence of extraneous noise, altering the photon count changes the strong and weak coupling spacings (see Fig. 3.5(a)) as it alters the local maxima and shoulders of the axial-FIMs of the individual focal planes. More specifically, increasing the photon count from 100 photons to 8000 photons increases the strong coupling spacing from 0.34 μm to 0.44 μm (i.e. a 29% elongation). In addition, decreasing the readout noise also increases the strong and weak coupling spacings (see Fig. 3.5(b)). For example, reducing the standard deviation of the readout noise from 10 e$^-$/pixel to 1 e$^-$/pixel increases the strong coupling spacing from 0.36 μm to 0.46 μm (i.e. a 28% enhancement). The effect of background noise on the strong and weak coupling spacings is similar to the effect of readout noise and hence is omitted for brevity.

It is important to note that the effect of changing the photon count and extraneous noise on the strong and weak coupling spacings is not significant when compared to the effect of magnification, numerical aperture and emission wavelength. An intuitive explanation of this behavior is as follows. In the absence of extraneous noise, changing the photon count only scales the FIM (due to the linear dependence of the FIM on the photon count) and therefore does not change the locations of the local maxima and shoulders of the axial-FIM (for details see Eq. (3.1)). In the presence of extraneous noise, however, there is a nonlinear dependence of the FIM on the photon count. This nonlinear dependence, in addition to scaling the FIM, causes the observed slight change in the positions of the local maxima and shoulders of the axial-FIM.

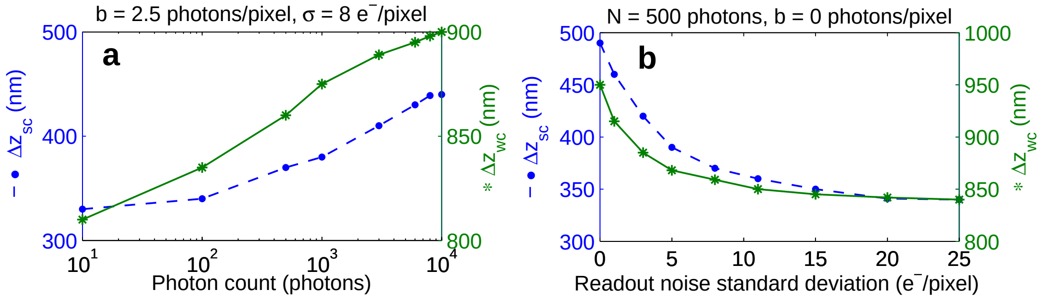

Figure 3.5: The effect of photon count and extraneous noise on the spacing scenarios. A plot of the strong coupling spacing (Δz_{sc}) and weak coupling spacing (Δz_{wc}) as a function of (a) the photon count (N) and (b) the standard deviation of the readout noise (σ). The ROI size is 32×32 pixels. The magnification is 100, the emission wavelength is 520 nm and the numerical aperture is 1.4. In (a), the background level and the standard deviation of the readout noise are 2.5 photons/pixel and 8 e^-/pixel, respectively. In (b), the photon count and the background level are 500 photons and 0 photons/pixel, respectively. Reprinted with permission from [31].

3.4.6 Spacing scenarios for MUM setups with more than two focal planes

In the previous sections, we described scenarios for adjusting the plane spacing for a 2-plane MUM setup that provide a relatively constant 3D localization accuracy along the z-axis. We next extend the spacing scenarios to MUM setups with more than two focal planes. The strong coupling spacing is obtained when the focal planes are positioned in such a way that the local maximum of the axial-FIM of a given plane overlaps with the zero of the axial-FIM of the adjacent plane. Figs. 3.6(a) and 3.6(b) show the axial-PLAM and the lateral-PLAM, respectively, for a 4-plane MUM setup with planes adjusted based on the strong coupling spacing. For the given set of imaging conditions, the axial-PLAM$_{MUM}$ and the lateral-PLAM vary from 23 nm to 30 nm and from 9.8 nm to 13 nm, respectively, over the z-range of [-0.2, 1.5] μm. This implies that the extension of the strong coupling spacing provides a relatively constant 3D localization accuracy along the z-axis.

The weak coupling spacing can be defined in an analogous way, i.e. the shoulder of the axial-FIM of one plane is selected to overlap with the zero of the axial-FIM of the adjacent plane. Figs. 3.6(c) and 3.6(d) show that the axial-PLAM$_{MUM}$ and the lateral-PLAM for

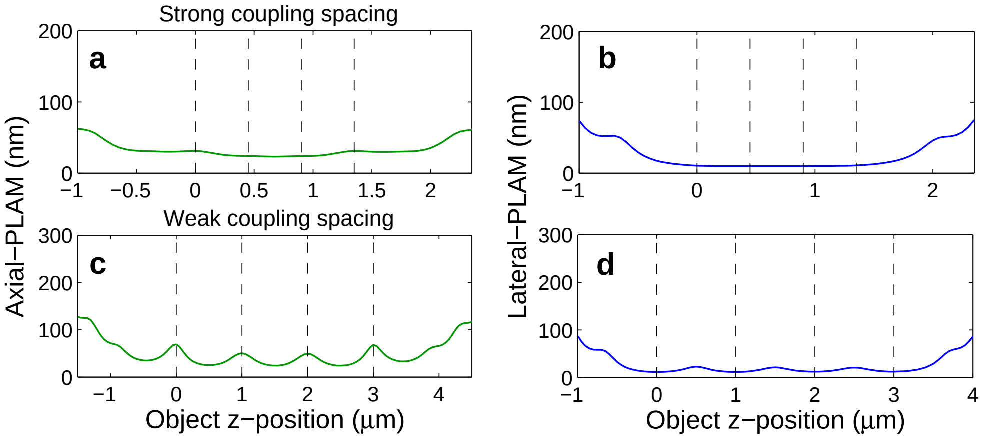

Figure 3.6: The strong and weak coupling spacings for a 4-plane MUM setup. (a) The axial-PLAM and (b) the lateral-PLAM as a function of the z-position of the point source for the strong coupling spacing for a 4-plane MUM setup. The planes are placed at 0, 0.45, 0.9 and 1.35 μm. (c) and (d) show the same for the weak coupling spacing for a 4-plane MUM setup where the planes are located at 0, 1, 2 and 3 μm. The magnification is 100, the numerical aperture is 1.3, the photon count is 250 photons/plane and the ROI size is 11 × 11 pixels. The emission wavelength is 520 nm. The background level and the standard deviation of the readout noise are 20 photons/pixel/plane and 3 e^-/pixel, respectively. Reprinted with permission from [31].

the extension of the weak coupling spacing are relatively constant along the z-axis as well. More specifically, the axial-PLAM$_{MUM}$ and the lateral-PLAM vary from 26 nm to 68 nm and from 11.6 nm to 22 nm, respectively, over the larger z-range of [-0.4, 3.4] μm.

3.4.7 Increasing the number of focal planes within a specific z-range does not necessarily enhance the localization accuracy along the z-axis

An important question in the design of MUM experiments concerns the appropriate number of focal planes that are required to cover a sample of a certain thickness. To address this concern, we next study the effect of changing the number of focal planes on the 3D localization accuracy of a MUM setup along the z-axis. Fig. 3.7(a) shows the axial-PLAM for MUM setups with 2 to 8 focal planes over the range of [-1, 1] μm, where the planes are placed based on the strong coupling spacing. We assume that the total photon count is fixed and is split equally among the focal planes. The axial-PLAM of the 2-plane setup has relatively small numerical values along the z-axis (see Fig. 3.7(a)). However, the values vary significantly (i.e, they vary from 34 nm to 67 nm over the z-range of [-1, 1] μm). By increasing the number of planes from 2 to 3, the numerical values of the axial-PLAM$_{MUM}$ increase while the curve becomes more flat (i.e. the axial-PLAM$_{MUM}$ varies from 37 nm to 56 nm over the same z-range).

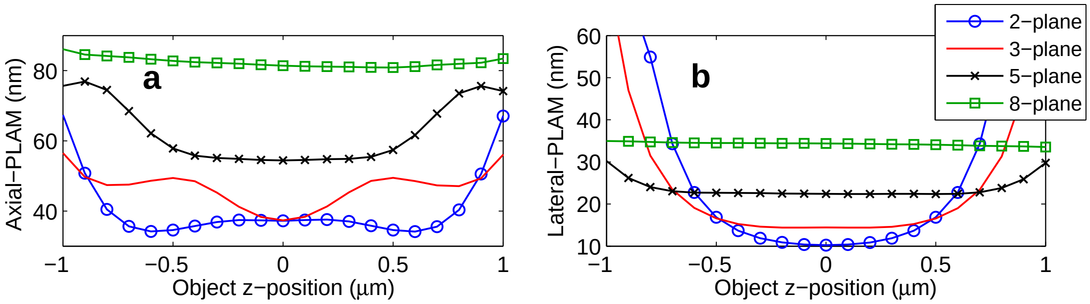

Figure 3.7: The effect of changing the number of focal planes on the 3D localization accuracy. (a) The axial-PLAM and (b) the lateral-PLAM for a MUM setup with different numbers of focal planes over a range of [-1, 1] μm. The magnification is 100, the numerical aperture is 1.3 and the ROI size is 11 × 11 pixels. The emission wavelength is 520 nm. The focal planes are located based on the strong coupling spacing. The total photon count is 1000 photons and is split equally among the focal planes. The background level and the standard deviation of the readout noise are 25 photons/pixel/plane and 8 e$^-$/pixel, respectively. Reprinted with permission from [31].

Further increasing the number of focal planes, e.g. to 5 or 8, yields more flat axial-PLAM$_{MUM}$ curves along the z-axis. For instance, for an 8-plane setup the axial-PLAM values vary from 81 nm to 86 nm over the same z-range. However, the numerical value of the axial-PLAM for a MUM setup with a large number of planes is consistently greater than that for a MUM setup with a small number of planes. A consistently large axial-PLAM$_{MUM}$ value implies a poor localization accuracy along the z-axis. Fig. 3.7(b) shows that the effect of changing the number of focal planes on the lateral-PLAM is analogous to its effect on the axial-PLAM$_{MUM}$.

An important implication of this behavior is that one can achieve a relatively constant

3D localization accuracy across the viewing and tracking depth by increasing the number of focal planes. However, as the number of focal planes increases, the numerical values of the localization accuracy become consistently large along the z-axis. The reason for this behavior is that by placing a large number of focal planes, the emitted light from the point source is split among the different planes such that the number of photons detected from the point source at each plane becomes relatively small when compared to the readout noise. This results in large numerical values in the axial-PLAM$_{MUM}$ and the lateral-PLAM which depend on the total number of detected photons per plane [26].

3.4.8 MUMDesignTool

To facilitate and speed up the tedious and time-consuming process of designing the focal plane spacing for a MUM setup, we developed a new software module, the MUMDesignTool[1] [31], which is incorporated with the recent release of our previously developed FandPLimitTool[2] [41]. The MUMDesignTool is developed in the MATLAB environment based on an object-oriented programming methodology and provides a user-friendly graphical user interface (see Fig. 3.8). Powered by two main working modes termed the *rapid mode* (noise-free) and the *precise mode* (corrupted by background, stochastic signal amplification and readout noise), the MUMDesignTool is capable of computing and plotting the 3D localization accuracy for MUM setups with up to 10 focal planes. The rapid mode allows the fast calculation of the 3D localization accuracy for a MUM setup by representing the FIM of the MUM setup in terms of the unit photon count FIM (uFIM) of the design focal plane (see Appendix C). This fast calculation is possible by assuming that the magnification is constant at different focal planes and that the data is devoid of extraneous noise sources. As a result, the rapid mode provides the ability to change the plane spacing, the number of focal planes and the photon count percentages in real-time, and to simultaneously visualize the FIM and PLAM. On the other hand, the precise mode of the MUMDesignTool calculates the 3D localization accuracy without considering the

---

[1] The software package is available at http://www.wardoberlab.com/software/mumdesigntool/.

[2] For more information visit http://www.wardoberlab.com/software/fandplimittool/.

assumptions made in the rapid mode (i.e. this mode directly computes Eq. (3.2)).

In addition, the MUMDesignTool is capable of exporting the results and acquisition parameters as image and text files, respectively. An approach to designing the plane spacing using this package is to first use the rapid mode to interactively change the plane spacing and the number of planes and visualize the behavior of the PLAM. This helps to find a candidate for one of the introduced spacing scenarios. The next step is then to run the precise mode with the extraneous noise parameters, and the spacings found in the rapid mode to ensure that the designed spacings are appropriate in the presence of noise.

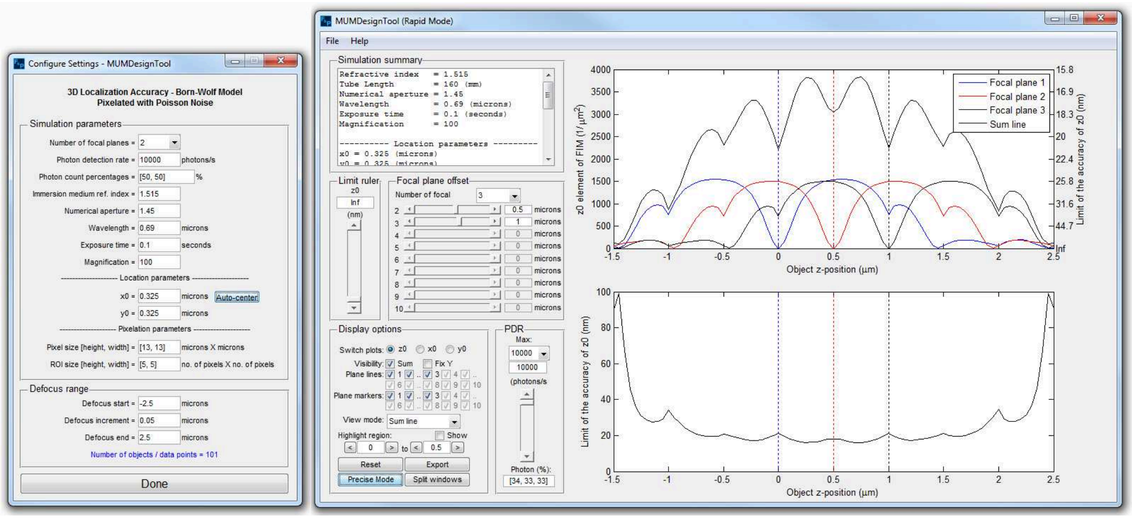

Configure Settings - MUMDesignTool

3D Localization Accuracy - Born-Wolf Model
Pixelated with Poisson Noise

Simulation parameters

Number of focal planes = 2
Photon detection rate = 10000 photons/s
Photon count percentages = [50, 50] %
Immersion medium ref. index = 1.515
Numerical aperture = 1.45
Wavelength = 0.69 microns
Exposure time = 0.1 seconds
Magnification = 100

------------------- Location parameters -------------------

x0 = 0.325 microns
y0 = 0.325 microns

------------------- Pixelation parameters -------------------

Pixel size [height, width] = [13, 13] microns X microns
ROI size [height, width] = [5, 5] no. of pixels X no. of pixels

Defocus range

Defocus start = -2.5 microns
Defocus increment = 0.05 microns
Defocus end = 2.5 microns
Number of objects / data points = 101

MUMDesignTool (Rapid Mode)

Simulation summary

```
Refractive index   = 1.515
Tube Length        = 160 (mm)
Numerical aperture = 1.45
Wavelength         = 0.69 (microns)
Exposure time      = 0.1 (seconds)
Magnification      = 100

---------- Location parameters ---------
x0 = 0.325 (microns)
y0 = 0.325 (microns)
```

Limit ruler z0: Inf (nm)

Focal plane offset

Number of focal: 3
2: 0.5 microns
3: 1 microns
4: 0 microns
5: 0 microns
6: 0 microns
7: 0 microns
8: 0 microns
9: 0 microns
10: 0 microns

Display options

Switch plots: ● z0 ○ x0 ○ y0
Visibility: ☑ Sum ☐ Fix Y
Plane lines: ☑ 1 ☑ .. ☑ 3 ☑ 4 ☑ .. ☑ 6 ☑ .. ☑ 8 ☑ 9 ☑ 10
Plane markers: ☑ 1 ☑ .. ☑ 3 ☑ 4 ☑ .. ☑ 6 ☑ .. ☑ 8 ☑ 9 ☑ 10
View mode: Sum line
Highlight region: 0 to 0.5 ☐ Show

PDR

Max: 10000
10000 (photons/s
Photon (%): [34, 33, 33]

Figure 3.8: The graphical user interface of the MUMDesignTool. The left and right panels show the configure settings and the rapid mode windows of the MUMDesignTool. Reprinted with permission from [37].

4. CONCLUSIONS

In this dissertation, we studied the performance limits of single molecule fluorescence microscopy in two and three dimensions. Our main contribution was twofold. First, we proposed an approach to determining the limit of the accuracy with which a general subcellular object, imaged using a fluorescence microscope, can be localized directly from an experimental image set. This technique, unlike traditional methods, does not rely on an analytical expression for the image of the object and therefore avoids potential model and parameter mismatch issues. The proposed technique is based on B-splines due to their important properties such as affine invariance, local support and positivity. We studied in detail a special case where the object of interest is a point source and, as such, the experimental image set pertains to an experimental PSF. We verified our approach using simulations and reported practical and non-point source examples. These developments can help to optimize the design of fluorescence microscopy experiments in practical conditions and in the presence of optical aberrations.

Second, we explored the problems encountered when designing MUM experiments. To address such problems, we developed techniques based on the Fisher information matrix for the appropriate selection of the number of focal planes and their spacings for a MUM setup. We further reported spacing scenarios called strong coupling and weak coupling which yield an appropriate 3D localization accuracy along the z-axis. This is of practical importance since it helps to estimate the locations of subcellular objects with a uniform level of accuracy across the specimen. To gain a better understanding of the effect of imaging conditions on the plane spacings, we investigated the effect of numerical aperture, magnification, photon count, emission wavelength and extraneous noise on the developed spacing scenarios. In addition, we studied the effect of changing the number of focal planes on the 3D localization accuracy and explored how this can help to design imaging experiments for covering thick samples. We also introduced a software package, the MUMDesignTool, to find appropriate plane spacings for a MUM setup. These developments should assist in optimizing 3D single molecule fluorescence microscopy experiments.

REFERENCES

[1] R. J. Ober, A. Tahmasbi, S. Ram, Z. Lin, and E. S. Ward, "Quantitative aspects of single molecule microscopy: Information-theoretic analysis of single-molecule data," *IEEE Signal Process. Mag.*, vol. 32, pp. 58–69, 2015.

[2] W. E. Moerner, "New directions in single-molecule imaging and analysis," *Proc. Natl. Acad. Sci. USA*, vol. 104, no. 31, pp. 12596–12602, 2007.

[3] J. W. Lichtman and J.-A. Conchello, "Fluorescence microscopy," *Nat. Methods*, vol. 2, no. 12, pp. 910–919, 2005.

[4] E. Meijering, I. Smal, and G. Danuser, "Tracking in molecular bioimaging," *IEEE Signal Process. Mag.*, vol. 23, pp. 46–53, May 2006.

[5] N. Chenouard, I. Smal, F. De Chaumont, M. Maška, I. F. Sbalzarini, Y. Gong, J. Cardinale, C. Carthel, S. Coraluppi, M. Winter, *et al.*, "Objective comparison of particle tracking methods," *Nat. Methods*, vol. 11, no. 3, pp. 281–289, 2014.

[6] M. Chalfie, Y. Tu, G. Euskirchen, W. Ward, and D. Prasher, "Green fluorescent protein as a marker for gene expression," *Science*, vol. 263, no. 5148, pp. 802–805, 1994.

[7] N. C. Shaner, R. E. Campbell, P. A. Steinbach, B. N. Giepmans, A. E. Palmer, and R. Y. Tsien, "Improved monomeric red, orange and yellow fluorescent proteins derived from discosoma sp. red fluorescent protein," *Nat. Biotechnol.*, vol. 22, no. 12, pp. 1567–1572, 2004.

[8] X. Michalet, F. Pinaud, L. Bentolila, J. Tsay, S. Doose, J. Li, G. Sundaresan, A. Wu, S. Gambhir, and S. Weiss, "Quantum dots for live cells, in vivo imaging, and diagnostics," *Science*, vol. 307, no. 5709, pp. 538–544, 2005.

[9] D. S. Lidke and K. A. Lidke, "Advances in high-resolution imaging–techniques for three-dimensional imaging of cellular structures," *J. Cell. Sci.*, vol. 125, no. 11,

pp. 2571–2580, 2012.

[10] M. Born and E. Wolf, *Principles of Optics.* Cambridge, UK: Cambridge University Press, seventh ed., 2002.

[11] X. Qu, D. Wu, L. Mets, and N. F. Scherer, "Nanometer-localized multiple single-molecule fluorescence microscopy," *Proc. Natl. Acad. Sci. USA*, vol. 101, no. 31, pp. 11298–11303, 2004.

[12] S. Ram, E. S. Ward, and R. J. Ober, "A stochastic analysis of performance limits for optical microscopes," *Multidim. Sys. Sig. Proc.*, vol. 17, pp. 27–57, 2006.

[13] R. J. Ober, S. Ram, and E. S. Ward, "Localization accuracy in single-molecule microscopy," *Biophys. J.*, vol. 86, pp. 1185–1200, 2004.

[14] W. E. Moerner and L. Kador, "Optical detection and spectroscopy of single molecules in a solid," *Phys. Rev. Lett.*, vol. 62, no. 21, p. 2535, 1989.

[15] M. Orrit and J. Bernard, "Single pentacene molecules detected by fluorescence excitation in a p-terphenyl crystal," *Phys. Rev. Lett.*, vol. 65, no. 21, p. 2716, 1990.

[16] W. Ambrose and W. Moerner, "Fluorescence spectroscopy and spectral diffusion of single impurity molecules in a crystal," *Nature*, vol. 349, no. 6306, pp. 225–227, 1991.

[17] A. Yildiz, J. N. Forkey, S. A. McKinney, T. Ha, Y. E. Goldman, and P. R. Selvin, "Myosin v walks hand-over-hand: single fluorophore imaging with 1.5-nm localization," *Science*, vol. 300, no. 5628, pp. 2061–2065, 2003.

[18] R. M. Dickson, A. B. Cubitt, R. Y. Tsien, and W. Moerner, "On/off blinking and switching behaviour of single molecules of green fluorescent protein," *Nature*, vol. 388, no. 6640, pp. 355–358, 1997.

[19] R. J. Ober, C. Martinez, X. Lai, J. Zhou, and E. S. Ward, "Exocytosis of igg as mediated by the receptor, fcrn: an analysis at the single-molecule level," *Proc. Natl. Acad. Sci. USA*, vol. 101, no. 30, pp. 11076–11081, 2004.

[20] S. Ram, E. S. Ward, and R. J. Ober, "Beyond rayleigh's criterion: a resolution measure with application to single-molecule microscopy," *Proc. Natl. Acad. Sci. USA*, vol. 103, no. 12, pp. 4457–4462, 2006.

[21] K. A. Lidke, B. Rieger, T. M. Jovin, and R. Heintzmann, "Superresolution by localization of quantum dots using blinking statistics," *Opt. Express*, vol. 13, no. 18, pp. 7052–7062, 2005.

[22] A. Van Oijen, J. Köhler, J. Schmidt, M. Müller, and G. Brakenhoff, "3-dimensional super-resolution by spectrally selective imaging," *Chem. Phys. Lett.*, vol. 292, no. 1, pp. 183–187, 1998.

[23] E. Betzig, G. H. Patterson, R. Sougrat, O. W. Lindwasser, S. Olenych, J. S. Bonifacino, M. W. Davidson, J. Lippincott-Schwartz, and H. F. Hess, "Imaging intracellular fluorescent proteins at nanometer resolution," *Science*, vol. 313, pp. 1642–1645, 2006.

[24] M. J. Rust, M. Bates, and X. Zhuang, "Sub-diffraction-limit imaging by stochastic optical reconstruction microscopy (storm)," *Nat. Methods*, vol. 3, no. 10, pp. 793–796, 2006.

[25] S. T. Hess, T. P. Girirajan, and M. D. Mason, "Ultra-high resolution imaging by fluorescence photoactivation localization microscopy," *Biophys. J.*, vol. 91, no. 11, pp. 4258–4272, 2006.

[26] S. Ram, P. Prabhat, J. Chao, E. S. Ward, and R. J. Ober, "High accuracy 3d quantum dot tracking with multifocal plane microscopy for the study of fast intracellular dynamics in live cells," *Biophys. J.*, vol. 95, pp. 6025–6043, 2008.

[27] M. K. Cheezum, W. F. Walker, and W. H. Guilford, "Quantitative comparison of algorithms for tracking single fluorescent particles," *Biophys. J.*, vol. 81, no. 4, pp. 2378–2388, 2001.

[28] X. Michalet, "Mean square displacement analysis of single-particle trajectories with localization error: Brownian motion in an isotropic medium," *Phys. Rev. E*, vol. 82, no. 4, p. 041914, 2010.

[29] C. S. Smith, N. Joseph, B. Rieger, and K. A. Lidke, "Fast, single-molecule localization that achieves theoretically minimum uncertainty," *Nat. Methods*, vol. 7, no. 5, pp. 373–375, 2010.

[30] H. Deschout, F. C. Zanacchi, M. Mlodzianoski, A. Diaspro, J. Bewersdorf, S. T. Hess, and K. Braeckmans, "Precisely and accurately localizing single emitters in fluorescence microscopy," *Nat. Methods*, vol. 11, pp. 253–266, 2014.

[31] A. Tahmasbi, S. Ram, J. Chao, A. V. Abraham, F. W. Tang, E. S. Ward, and R. J. Ober, "Designing the focal plane spacing for multifocal plane microscopy," *Opt. Express*, vol. 22, pp. 16706–16721, 2014.

[32] S. Ram, D. Kim, R. J. Ober, and E. S. Ward, "3d single molecule tracking with multifocal plane microscopy reveals rapid intercellular transferrin transport at epithelial cell barriers," *Biophys. J.*, vol. 103, no. 7, pp. 1594–1603, 2012.

[33] S. F. Gibson and F. Lanni, "Experimental test of an analytical model of aberration in an oil-immersion objective lens used in three-dimensional light microscopy," *J. Opt. Soc. Am. A*, vol. 9, pp. 154–166, 1992.

[34] A. Tahmasbi, E. S. Ward, and R. J. Ober, "Determination of localization accuracy based on experimentally acquired image sets: applications to single molecule microscopy," *Opt. Express*, vol. 23, pp. 7630–7652, 2015.

[35] P. Torok and F. J. Kao, *Optical Imaging and Microscopy.* New York, NY: Springer Verlag, first ed., 2003.

[36] P. Prabhat, S. Ram, E. S. Ward, and R. J. Ober, "Simultaneous imaging of different focal planes in fluorescence microscopy for the study of cellular dynamics in three dimensions," *IEEE Trans. Nanobiosci.*, vol. 3, pp. 237–242, 2004.

[37] A. Tahmasbi, S. Ram, J. Chao, A. V. Abraham, E. S. Ward, and R. J. Ober, "An information-theoretic approach to designing the plane spacing for multifocal plane microscopy," in *Proc. SPIE*, vol. 9330, p. 933011, 2015.

[38] M. Unser, A. Aldroubi, and M. Eden, "B-spline signal processing: Part i–theory," *IEEE Trans. Signal Process.*, vol. 41, pp. 821–832, 1993.

[39] W. E. Moerner and D. P. Fromm, "Methods of single-molecule fluorescence spectroscopy and microscopy," *Rev. Sci. Instrum.*, vol. 74, no. 8, pp. 3597–3619, 2003.

[40] A. Small and S. Stahlheber, "Fluorophore localization algorithms for super-resolution microscopy," *Nat. Methods*, vol. 11, pp. 267–279, 2014.

[41] A. V. Abraham, S. Ram, J. Chao, E. S. Ward, and R. J. Ober, "Quantitative study of single molecule location estimation techniques," *Opt. Express*, vol. 17, pp. 23352–23373, 2009.

[42] S. M. Kay, *Fundamentals of Statistical Signal Processing: Estimation Theory.* Upper Saddle River, NJ: Prentice Hall PTR, first ed., 1993.

[43] D. L. Snyder and M. I. Miller, *Random Point Processes in Time and Space.* New York, NY: Springer Verlag, second ed., 1991.

[44] M. Badieirostami, M. D. Lew, M. A. Thompson, and W. E. Moerner, "Three-dimensional localization precision of the double-helix point spread function versus astigmatism and biplane," *Appl. Phys. Lett.*, vol. 97, p. 161103, 2010.

[45] Y. Shechtman, S. J. Sahl, A. S. Backer, and W. E. Moerner, "Optimal point spread function design for 3d imaging," *Phys. Rev. Lett.*, vol. 113, no. 13, p. 133902, 2014.

[46] F. Aguet, S. Geissbühler, I. Märki, T. Lasser, and M. Unser, "Super-resolution orientation estimation and localization of fluorescent dipoles using 3-d steerable filters," *Opt. Express*, vol. 17, pp. 6829–6848, Apr 2009.

[47] X. Michalet and A. J. Berglund, "Optimal diffusion coefficient estimation in single-particle tracking," *Phys. Rev. E*, vol. 85, no. 6, p. 061916, 2012.

[48] B. Zhang, J. Zerubia, and J. C. Olivo-Marin, "Gaussian approximations of fluorescence microscope point-spread function models," *Appl. Opt.*, vol. 46, pp. 1819–1829, 2007.

[49] M. Unser, "Splines: a perfect fit for signal and image processing," *IEEE Signal Process. Mag.*, vol. 16, pp. 22–38, 1999.

[50] C. D. Boor, *A Practical Guide to Splines.* New York, NY: Springer-Verlag, rev. ed., 2001.

[51] I. J. Schoenberg, "Cardinal interpolation and spline functions," *J. Approx. Theory*, vol. 2, no. 2, pp. 167–206, 1969.

[52] M. Arigovindan, M. Sühling, P. Hunziker, and M. Unser, "Variational image reconstruction from arbitrarily spaced samples: A fast multiresolution spline solution," *IEEE Trans. Image Process.*, vol. 14, no. 4, pp. 450–460, 2005.

[53] A. Tahmasbi, E. S. Ward, and R. J. Ober, "New results on the single molecule localization problem in two and three dimensions," in *Proc. SPIE*, vol. 9554, pp. 955402–955402–8, 2015.

[54] X. Lai, Z. Lin, E. S. Ward, and R. J. Ober, "Noise suppression of point spread functions and its influence on deconvolution of three-dimensional fluorescence microscopy image sets," *J. Microsc.*, vol. 217, pp. 93–108, 2005.

[55] C. D. Claxton and R. C. Staunton, "Measurement of the point-spread function of a noisy imaging system," *J. Opt. Soc. Am. A*, vol. 25, pp. 159–170, 2008.

[56] M. Baranski, S. Perrin, N. Passilly, L. Froehly, J. Albero, S. Bargiel, and C. Gorecki, "A simple method for quality evaluation of micro-optical components based on 3d ipsf measurement," *Opt. Express*, vol. 22, no. 11, pp. 13202–13212, 2014.

[57] S. R. P. Pavani and R. Piestun, "Three dimensional tracking of fluorescent microparticles using a photon-limited double-helix response system," *Opt. Express*, vol. 16, no. 26, pp. 22048–22057, 2008.

[58] S. Ram, P. Prabhat, E. S. Ward, and R. J. Ober, "Improved single particle localization accuracy with dual objective multifocal plane microscopy," *Opt. Express*, vol. 17, pp. 6881–6898, Apr 2009.

[59] R. E. Campbell, O. Tour, A. E. Palmer, P. A. Steinbach, G. S. Baird, D. A. Zacharias, and R. Y. Tsien, "A monomeric red fluorescent protein," *Proc. Natl. Acad. Sci. USA*, vol. 99, no. 12, pp. 7877–7882, 2002.

[60] J. Chao, E. S. Ward, and R. J. Ober, "Fisher information matrix for branching processes with application to electron-multiplying charge-coupled devices," *Multidim. Sys. Sig. Proc.*, vol. 23, pp. 349–379, 2012.

[61] S. Liu, E. Kromann, W. Krueger, J. Bewersdorf, and K. Lidke, "Three dimensional single molecule localization using a phase retrieved pupil function," *Opt. Express*, vol. 21, pp. 29462–29487, 2013.

[62] S. Quirin, S. R. P. Pavani, and R. Piestun, "Optimal 3d single-molecule localization for superresolution microscopy with aberrations and engineered point spread functions," *Proc. Natl. Acad. Sci. USA*, vol. 109, pp. 675–679, 2012.

[63] P. M. Blanchard and A. H. Greenaway, "Simultaneous multiplane imaging with a distorted diffraction grating," *Appl. Opt.*, vol. 38, no. 32, pp. 6692–6699, 1999.

[64] S. Ram, J. Chao, P. Prabhat, E. S. Ward, and R. J. Ober, "Overcoming the depth discrimination barrier in widefield microscopes: 3d single molecule tracking with high axial accuracy," in *Proc. SPIE*, vol. 6862, pp. 68620O–68620O–7, 2008.

[65] L. Dehmelt and P. I. H. Bastiaens, "Spatial organization of intracellular communication: insights from imaging," *Nature Rev. Mol. Cell Biol.*, vol. 11, pp. 440–452, 2010.

[66] A. Jesacher, C. Roider, and M. Ritsch-Marte, "Enhancing diffractive multi-plane microscopy using colored illumination," *Opt. Express*, vol. 21, no. 9, pp. 11150–11161, 2013.

[67] S. Wolter, A. Löschberger, T. Holm, S. Aufmkolk, M.-C. Dabauvalle, S. van de Linde, and M. Sauer, "Rapidstorm: accurate, fast open-source software for localization microscopy," *Nat. Methods*, vol. 9, no. 11, pp. 1040–1041, 2012.

[68] H. Kirshner, F. Aguet, D. Sage, and M. Unser, "3-d psf fitting for fluorescence microscopy: implementation and localization application," *J. Microsc.*, vol. 249, no. 1, pp. 13–25, 2013.

[69] P. A. Dalgarno, H. I. C. Dalgarno, A. Putoud, R. Lambert, L. Paterson, D. C. Logan, D. P. Towers, R. J. Warburton, and A. H. Greenaway, "Multiplane imaging and three dimensional nanoscale particle tracking in biological microscopy," *Opt. Express*, vol. 18, no. 2, pp. 877–884, 2010.

[70] Z. Gan, S. Ram, R. J. Ober, and E. S. Ward, "Using multifocal plane microscopy to reveal novel trafficking processes in the recycling pathway," *J. Cell Sci.*, vol. 126, no. 5, pp. 1176–1188, 2013.

[71] P. Prabhat, Z. Gan, J. Chao, S. Ram, C. Vaccaro, S. Gibbons, R. J. Ober, and E. S. Ward, "Elucidation of intracellular recycling pathways leading to exocytosis of the fc receptor, fcrn, by using multifocal plane microscopy," *Proc. Natl. Acad. Sci. USA*, vol. 104, no. 14, pp. 5889–5894, 2007.

[72] S. Abrahamsson, J. Chen, B. Hajj, S. Stallinga, A. Y. Katsov, J.Wisniewski, G. Mizuguchi, P. Soule, F. Mueller, C. D. Darzacq, X. Darzacq, C. Wu, C. I. Bargmann, D. A. Agard, M. Dahan, and M. G. L. Gustafsson, "Fast multicolor 3d imaging using aberration-corrected multifocus microscopy," *Nat. Methods*, vol. 10, pp. 60–63, 2013.

[73] S. Ram, E. S. Ward, and R. J. Ober, "How accurately can a single molecule be localized in three dimensions using a fluorescence microscope?," in *Proc. SPIE*, vol. 5699, pp. 426–435, 2005.

[74] C. R. Rao, *Linear Statistical Inference and its Applications.* New York, NY: John Wiley & Sons, 1965.

[75] L. Tao and C. Nicholson, "The three-dimensional point spread functions of a microscope objective in image and object space," *J. Microsc.*, vol. 178, no. 3, pp. 267–271, 1995.

APPENDIX A

INTEGRAL OF B-SPLINES OVER THE REAL LINE

Let $\beta^d(x),\ x \in \mathbb{R}$ be the B-spline function of degree $d \in \mathbb{N}_0$ and let $\Delta x_0 > 0$. We aim to show,

$$\int_{\mathbb{R}} \beta^d\left(\frac{x}{\Delta x_0} - n\right) dx = \Delta x_0 \int_{\mathbb{R}} \beta^d(v)\, dv = \Delta x_0, \qquad n = 1, \ldots, K_{\text{col}},$$

where $v := x/\Delta x_0 - n$ and, therefore, $dx = \Delta x_0 dv$.

Obviously, the above equality holds if $\int_{\mathbb{R}} \beta^d(x)dx = 1$ for $d \in \mathbb{N}_0$. We next prove this by induction. As a base case assume $d = 0$, then from the definition of the B-spline function (see Eq. (2.6)) we have

$$\begin{aligned}\int_{\mathbb{R}} \beta^0(x)dx &= \int_{\mathbb{R}} \sum_{j=0}^{1} \frac{(-1)^j}{1!} \binom{1}{j} \left(x + \frac{1}{2} - j\right)^0 u\left(x + \frac{1}{2} - j\right) dx \\ &= \int_{\mathbb{R}} u\left(x + \frac{1}{2}\right) - u\left(x - \frac{1}{2}\right) dx = \int_{-\frac{1}{2}}^{\frac{1}{2}} dx = 1.\end{aligned}$$

For the induction step, let $k \in \mathbb{N}_0$ and suppose $\int_{\mathbb{R}} \beta^k(x)dx = 1$ is true. Denote by $*$ the convolution operator. Then

$$\int_{\mathbb{R}} \beta^{k+1}(x)dx = \int_{\mathbb{R}} \beta^k(x) * \beta^0(x)dx = \int_{\mathbb{R}} \beta^k(x)dx \times \int_{\mathbb{R}} \beta^0(x)dx = 1 \times 1 = 1,$$

where we used the recursive formula of B-splines [49,51] and applied the general result that the integral of the convolution of two integrable functions on the entire space is obtained as the product of their integrals. We then used the induction hypothesis and the result of the base case. Thus, $\int_{\mathbb{R}} \beta^d(x)dx = 1$ holds for $d = k + 1$, and the proof of the induction step is complete.

APPENDIX B

DERIVATION OF THE PARTIAL DERIVATIVES

In this section, we derive the expressions for the partial derivatives of $\mu_\theta(k),\ k = 1,\ldots,K_{\text{pix}}$, w.r.t. the unknown parameters. Taking the partial derivatives of both sides of Eq. (2.14) w.r.t. x_0, we have

$$\begin{aligned}
\frac{\partial \mu_\theta(k)}{\partial x_0} &\approx \frac{\partial}{\partial x_0}\frac{N}{M^2}\int_{C_k}\sum_{m,n,p}\tilde{a}^{z_0}_{m,n,p}\beta^d\left(\frac{\frac{x}{M}-x_0}{\Delta x_0}-n\right)\beta^d\left(\frac{\frac{y}{M}-y_0}{\Delta y_0}-m\right)\beta^d\left(\frac{z_0}{\Delta z_0}-p\right)d\boldsymbol{r}\\
&= \frac{N}{M^2}\int_{C_k}\sum_{m,n,p}\tilde{a}^{z_0}_{m,n,p}\frac{\partial\beta^d\left(\frac{\frac{x}{M}-x_0}{\Delta x_0}-n\right)}{\partial x_0}\beta^d\left(\frac{\frac{y}{M}-y_0}{\Delta y_0}-m\right)\beta^d\left(\frac{z_0}{\Delta z_0}-p\right)d\boldsymbol{r}\\
&= \frac{-N}{M^2\Delta x_0}\sum_{p=1}^{K_{\text{stk}}}\beta^d\left(\frac{z_0}{\Delta z_0}-p\right)\int_{C_k}\sum_{m=1}^{K_{\text{row}}}\beta^d\left(\frac{\frac{y}{M}-y_0}{\Delta y_0}-m\right)\times\\
&\qquad\underbrace{\sum_{n=1}^{K_{\text{col}}}\tilde{a}^{z_0}_{m,n,p}\left(\beta^{d-1}\left(\frac{\frac{x}{M}-x_0}{\Delta x_0}-n+\frac{1}{2}\right)-\beta^{d-1}\left(\frac{\frac{x}{M}-x_0}{\Delta x_0}-n-\frac{1}{2}\right)\right)}_{T1}d\boldsymbol{r}, \qquad \text{(B.1)}
\end{aligned}$$

where $\boldsymbol{r} = (x, y) \in \mathbb{R}^2$ and the last equation was derived by making use of Eq. (2.15). For conciseness, define $u := (\frac{x}{M} - x_0)/\Delta x_0$. The term $T1$ in the above expression can be simplified as

$$T1 = \underbrace{\sum_{n=1}^{K_{\text{col}}}\tilde{a}^{z_0}_{m,n,p}\beta^{d-1}\left(u-n+\frac{1}{2}\right)}_{A} - \underbrace{\sum_{n=1}^{K_{\text{col}}}\tilde{a}^{z_0}_{m,n,p}\beta^{d-1}\left(u-n-\frac{1}{2}\right)}_{B}, \qquad \text{(B.2)}$$

where assuming that $\tilde{a}_{m,K_{\text{col}}+1,p} = 0,\ m = 1,\ldots,K_{\text{row}},\ p = 1,\ldots,K_{\text{stk}}$,

$$A = \sum_{n=1}^{K_{\text{col}}}\tilde{a}^{z_0}_{m,n,p}\beta^{d-1}\left(u-n+\frac{1}{2}\right) = \sum_{n=1}^{K_{\text{col}}+1}\tilde{a}^{z_0}_{m,n,p}\beta^{d-1}\left(u-n+\frac{1}{2}\right). \qquad \text{(B.3)}$$

In addition, by defining $j = n + 1$ we have

$$B = \sum_{j=2}^{K_{\text{col}}+1} \tilde{a}^{z_0}_{m,j-1,p} \beta^{d-1}\left(u - (j-1) - \frac{1}{2}\right) = \sum_{j=1}^{K_{\text{col}}+1} \tilde{a}^{z_0}_{m,j-1,p} \beta^{d-1}\left(u - j + \frac{1}{2}\right), \tag{B.4}$$

where the last identity is true assuming that $\tilde{a}_{m,0,p} = 0,\ m = 1, \ldots, K_{\text{row}},\ p = 1, \ldots, K_{\text{stk}}$. Substituting (B.3) and (B.4) into (B.2) it follows

$$T1 = \sum_{n=1}^{K_{\text{col}}+1} \left(\tilde{a}^{z_0}_{m,n,p} - \tilde{a}^{z_0}_{m,n-1,p}\right) \beta^{d-1}\left(u - n + \frac{1}{2}\right).$$

By substituting the above expression into Eq. (B.1), for $k = 1, \ldots, K_{\text{pix}}$, we finally have

$$\begin{aligned} \frac{\partial \mu_\theta(k)}{\partial x_0} &\approx \frac{-N}{M^2} \sum_{m=1}^{K_{\text{row}}} \sum_{n=1}^{K_{\text{col}}+1} \sum_{p=1}^{K_{\text{stk}}} \frac{\tilde{a}^{z_0}_{m,n,p} - \tilde{a}^{z_0}_{m,n-1,p}}{\Delta x_0} \beta^d\left(\frac{z_0}{\Delta z_0} - p\right) \\ &\quad \times \int_{C_k} \beta^{d-1}\left(\frac{\frac{x}{M} - x_0}{\Delta x_0} - n + \frac{1}{2}\right) \beta^d\left(\frac{\frac{y}{M} - y_0}{\Delta y_0} - m\right) d\boldsymbol{r}, \end{aligned}$$

where $\boldsymbol{r} = (x, y) \in \mathbb{R}^2$, $\tilde{a}^{z_0}_{m,0,p} = \tilde{a}^{z_0}_{m,K_{\text{col}}+1,p} = 0$, for all $m = 1, \ldots, K_{\text{row}}$, and $p = 1, \ldots, K_{\text{stk}}$. The partial derivative w.r.t. y_0 can be derived in the same way.

For the derivation of the partial derivative of μ_θ w.r.t. z_0, we note that the normalization constant C is also a function of the z_0. Taking the partial derivatives of both sides of Eq. (2.14) w.r.t. $z_0 \in \mathbb{R}$, we have

$$\begin{aligned} \frac{\partial \mu_\theta(k)}{\partial z_0} &\approx \frac{\partial}{\partial z_0} \frac{\frac{N}{M^2} \int_{C_k} \hat{s}^d_a\left(\frac{x}{M} - x_0, \frac{y}{M} - y_0, z_0\right) d\boldsymbol{r}}{C(z_0)} \\ &= G_\theta(k) - \frac{1}{C^2(z_0)} \frac{\partial C(z_0)}{\partial z_0} \frac{N \int_{C_k} \hat{s}^d_a\left(\frac{x}{M} - x_0, \frac{y}{M} - y_0, z_0\right) d\boldsymbol{r}}{M^2} \\ &= G_\theta(k) - \frac{1}{C(z_0)} \frac{\partial C(z_0)}{\partial z_0} \mu_\theta(k), \end{aligned} \tag{B.5}$$

for $k = 1, \ldots, K_{\text{pix}}$, where

$$G_\theta(k) := \frac{N}{M^2 C(z_0)} \int_{C_k} \frac{\partial}{\partial z_0} \hat{s}^d_a\left(\frac{x}{M} - x_0, \frac{y}{M} - y_0, z_0\right) d\boldsymbol{r}, \qquad k = 1, \ldots, K_{\text{pix}}.$$

The above expression can be simplified as follows

$$\begin{aligned}
G_\theta(k) &= \frac{N}{M^2 C(z_0)} \int_{C_k} \sum_{m,n,p} \hat{a}_{m,n,p} \beta^d \left(\frac{\frac{x}{M} - x_0}{\Delta x_0} - n \right) \beta^d \left(\frac{\frac{y}{M} - y_0}{\Delta y_0} - m \right) \\
&\qquad \times \frac{\partial \beta^d \left(\frac{z_0}{\Delta z_0} - p \right)}{\partial z_0} d\boldsymbol{r} \\
&= \frac{N}{M^2 C(z_0) \Delta z_0} \int_{C_k} \sum_{m=1}^{K_{\text{row}}} \sum_{n=1}^{K_{\text{col}}} \beta^d \left(\frac{\frac{x}{M} - x_0}{\Delta x_0} - n \right) \beta^d \left(\frac{\frac{y}{M} - y_0}{\Delta y_0} - m \right) d\boldsymbol{r} \\
&\qquad \times \underbrace{\sum_{p=1}^{K_{\text{stk}}} \hat{a}_{m,n,p} \left(\beta^{d-1}(\frac{z_0}{\Delta z_0} - p + \frac{1}{2}) - \beta^{d-1}(\frac{z_0}{\Delta z_0} - p - \frac{1}{2}) \right)}_{T2},
\end{aligned} \tag{B.6}$$

where the last equation was derived by making use of Eq. (2.15). Assuming $\hat{a}_{m,n,0} = \hat{a}_{m,n,K_{\text{stk}}+1} = 0,\ m = 1, \ldots, K_{\text{row}},\ n = 1, \ldots, K_{\text{col}}$, it is straightforward to verify that

$$T2 = \sum_{p=1}^{K_{\text{stk}}+1} \left(\hat{a}_{m,n,p} - \hat{a}_{m,n,p-1} \right) \beta^{d-1} \left(\frac{z_0}{\Delta z_0} - p + \frac{1}{2} \right). \tag{B.7}$$

By substituting the above expression into Eq. (B.6), for $k = 1, \ldots, K_{\text{pix}}$, we have

$$\begin{aligned}
G_\theta(k) = \frac{N}{M^2} \sum_{m=1}^{K_{\text{row}}} \sum_{n=1}^{K_{\text{col}}} \sum_{p=1}^{K_{\text{stk}}+1} & \frac{\tilde{a}^{z_0}_{m,n,p} - \tilde{a}^{z_0}_{m,n,p-1}}{\Delta z_0} \beta^{d-1} \left(\frac{z_0}{\Delta z_0} - p + \frac{1}{2} \right) \\
& \times \int_{C_k} \beta^d \left(\frac{\frac{x}{M} - x_0}{\Delta x_0} - n \right) \beta^d \left(\frac{\frac{y}{M} - y_0}{\Delta y_0} - m \right) d\boldsymbol{r},
\end{aligned} \tag{B.8}$$

where $\boldsymbol{r} = (x, y) \in \mathbb{R}^2$, $\tilde{a}^{z_0}_{m,n,0} = \tilde{a}^{z_0}_{m,n,K_{\text{stk}}+1} = 0$, for all $m = 1, \ldots, K_{\text{row}}$, and $n = 1, \ldots, K_{\text{col}}$.

By making use of Eq. (2.13), the second term on the right-hand side of Eq. (B.5) can be simplified as follows

$$\begin{aligned}
\frac{1}{C(z_0)}\frac{\partial C(z_0)}{\partial z_0} &= \frac{\Delta x_0 \Delta y_0}{C(z_0)} \sum_{m,n,p} \hat{a}_{m,n,p} \frac{\partial}{\partial z_0} \beta^d \left(\frac{z_0}{\Delta z_0} - p \right) \\
&= \Delta x_0 \Delta y_0 \sum_{m,n,p} \tilde{a}^{z_0}_{m,n,p} \frac{\partial}{\partial z_0} \beta^d \left(\frac{z_0}{\Delta z_0} - p \right) \\
&= \frac{\Delta x_0 \Delta y_0}{\Delta z_0} \sum_{m=1}^{K_{\text{row}}} \sum_{n=1}^{K_{\text{col}}} \sum_{p=1}^{K_{\text{stk}}} \tilde{a}^{z_0}_{m,n,p} \left(\beta^{d-1}(\frac{z_0}{\Delta z_0} - p + \frac{1}{2}) - \beta^{d-1}(\frac{z_0}{\Delta z_0} - p - \frac{1}{2}) \right) \\
&= \frac{\Delta x_0 \Delta y_0}{\Delta z_0} \sum_{m=1}^{K_{\text{row}}} \sum_{n=1}^{K_{\text{col}}} \sum_{p=1}^{K_{\text{stk}}+1} (\tilde{a}^{z_0}_{m,n,p} - \tilde{a}^{z_0}_{m,n,p-1}) \beta^{d-1} \left(\frac{z_0}{\Delta z_0} - p + \frac{1}{2} \right),
\end{aligned}$$

where $z_0 \in \mathbb{R}$ and we made use of Eq. (2.15) and assumed $\tilde{a}^{z_0}_{m,n,0} = \tilde{a}^{z_0}_{m,n,K_{\text{stk}}+1} = 0$, for all $m = 1, \ldots, K_{\text{row}}$, and $n = 1, \ldots, K_{\text{col}}$. The last identity was derived in a similar way as Eq. (B.7). The result follows immediately by substituting Eq. (B.8) and the above equation into Eq. (B.5).

APPENDIX C

APPROXIMATE BUT FAST CALCULATION OF THE FIM

In Section 3.3.2, we discussed a graphical interpretation for the design of the focal plane spacing for a MUM system. Building on the same idea and by making additional assumptions, here we develop an approach for the fast calculation of the FIM for a MUM setup. We also discuss the additional assumptions and the resulting properties of the FIM that are exploited for the design process. This fast approach is also used in the rapid mode of the MUMDesignTool. In this mode of the software, the design process can be carried out graphically in real-time as it avoids the often very time-consuming calculations of the full computations.

From Eq. (2.1) we have $\mu_{\theta,n}(k) = N_n \tilde{\mu}_{\theta,n}(k)$. Assuming that the data is devoid of extraneous noise sources, $\nu_{\theta,n}(k) = \mu_{\theta,n}(k)$ and $\psi_n(k) = 1$ for $k = 1, \ldots, K_{pix},\ n = 1, \ldots, K_{pln}$. This assumption will prove to be useful for the fast calculation of the FIM for focal planes with different expected number of detected photons. Hence, from Eq. (3.1) it follows

$$\begin{aligned}\boldsymbol{I}_n(\theta) &= \sum_{k=1}^{K_{pix}} \frac{1}{N_n \tilde{\mu}_{\theta,n}(k)} \left(\frac{\partial \left(N_n \tilde{\mu}_{\theta,n}(k) \right)}{\partial \theta} \right)^T \frac{\partial \left(N_n \tilde{\mu}_{\theta,n}(k) \right)}{\partial \theta} \\ &= N_n \sum_{k=1}^{K_{pix}} \frac{1}{\tilde{\mu}_{\theta,n}(k)} \left(\frac{\partial \tilde{\mu}_{\theta,n}(k)}{\partial \theta} \right)^T \frac{\partial \tilde{\mu}_{\theta,n}(k)}{\partial \theta} := N_n \tilde{\boldsymbol{I}}_n(\theta), \quad \theta \in \Theta,\ n = 1, \ldots, K_{pln}.\end{aligned}$$

We refer to $\tilde{\boldsymbol{I}}_n(\theta) = \tilde{\boldsymbol{I}}_n(x_0, y_0, z_0),\ \theta = (x_0, y_0, z_0) \in \Theta$ as the uFIM of the n^{th} plane which is a function of M_n and $\Delta z_{1n},\ n = 1, \ldots, K_{pln}$. We now assume that the lateral magnification is the same for all focal planes, i.e. we suppose $M_n = M_1$ for all $n = 2, \ldots, K_{pln}$. Using this assumption it follows that $\tilde{\boldsymbol{I}}_n(\theta) = \tilde{\boldsymbol{I}}_n(x_0, y_0, z_0) = \tilde{\boldsymbol{I}}_1(x_0, y_0, z_0 - \Delta z_{1n}),\ n = 2, \ldots, K_{pln}$.

Combining this result with Eq. (3.2), we define the fast FIM$_{MUM}$ as

$$\begin{aligned}\tilde{\boldsymbol{I}}_{MUM}(\theta) :&= N_1\tilde{\boldsymbol{I}}_1(x_0, y_0, z_0) + N_2\tilde{\boldsymbol{I}}_1(x_0, y_0, z_0 - \Delta z_{12}) + \dots \\ &+ N_{K_{pln}}\tilde{\boldsymbol{I}}_1(x_0, y_0, z_0 - \Delta z_{1K_{pln}}), \qquad \theta = (x_0, y_0, z_0) \in \Theta,\end{aligned}$$

which is a weighted sum of the uFIM of the design focal plane evaluated at different z-positions. The above equation implies that, in this approximation setting, obtaining the FIM for a MUM setup for a range of z-positions only requires one calculation that is the uFIM of the design focal plane (i.e. $\tilde{\boldsymbol{I}}_1$) for the range of z-positions. On the other hand, from Eq. (3.2) obtaining the FIM for a MUM setup for the same range of z-positions using the precise approach requires $K_{pln} \times a$ calculations, where K_{pln} calculations are needed for the FIMs of the individual planes (i.e. $\boldsymbol{I}_1, \dots, \boldsymbol{I}_{K_{pln}}$) and a is the number of configurations to be tried when varying the plane spacing.

As a consequence, the rapid mode of the MUMDesignTool, which uses the above approximate approach, can significantly speed up the design procedure for the plane spacing for a MUM setup that is otherwise very time consuming using the precise method. However, it is important to note that the PLAM obtained using the rapid mode is valid under the assumptions that the observed data is devoid of extraneous noise and that the lateral magnification is the same for all focal planes. In a practical situation where the data is corrupted by extraneous noise, we recommend verifying the results of the fast calculations by performing the precise calculations (which correspond to the noisy case). The precise mode of the MUMDesignTool is capable of calculating the FIM and PLAM for a MUM setup in the presence of extraneous noise sources such as background, stochastic signal amplification and readout using the general expression given by Eq. (3.2). For this purpose, the FIM for each focal plane is calculated separately using Eq. (3.1).

If there is a significant discrepancy between the results of the rapid mode and the results of the precise mode, the plane spacing designed using the rapid mode (i.e. the candidate spacing) should be fine tuned. The fine tuning can be performed by slightly increasing and/or decreasing the candidate spacing and then rerunning the precise mode. The results of the precise mode for these slightly different spacings can then be compared to find the desired spacing (e.g. the spacing that provides the flattest axial-PLAM curve).

APPENDIX D

BIOGRAPHICAL STATEMENT

Amir Tahmasbi received the B.Sc. and M.Sc. degrees (with honors) both in Electrical Engineering from Shiraz University of Technology, Shiraz, Iran in 2008 and Iran University of Science and Technology (IUST), Tehran, Iran in 2010, respectively. He is currently pursuing his Ph.D. degree in Biomedical Engineering at Texas A&M University, College Station, TX, USA. From 2011 to 2014, he was a member of Ward Ober Lab, Department of Immunology, University of Texas Southwestern Medical Center, Dallas, TX. He is a past member of Opto-electronics and Machine Vision Lab, IUST. He was also a member of the Satellite Research Center, IUST, from 2009 to 2011 and collaborated in the design and development of the Navid and Zafar satellites.

Amir is a student member of IEEE, IEEE Signal Processing Society, IEEE Computer Society, and IEEE Engineering in Medicine and Biology Society. He has served as a reviewer in various refereed journals, namely IEEE Transactions on Cybernetics, and multiple international conferences. His research interests mostly lie in the fields of statistical signal processing and estimation theory, biomedical image analysis with applications to fluorescence microscopy and mammography, and real-time embedded digital signal processing.